# Intestinal Tissue Mechanics Regulate Angiogenesis and Stem Cell Proliferation via Vascular Piezo

**Jade A. Phillips[1‡], Jessica Perochon[2‡*], Cai T. Johnson[2,3], Matthew Walker[3,5], Colin Nixon[1], Mark Hughes[1], André Barros-Carvalho[4], Yachuan Yu[1], Louise Mitchell[1], Karen Blyth[1,2], Massimo Vassalli[3,5], Julia B. Cordero[1,2*]**

[1] CRUK Scotland Institute, Garscube Estate, Switchback Road, Glasgow, G61 1BD, U.K.

[2] School of Cancer Sciences, Wolfson Wohl Cancer Research Centre, University of Glasgow, Garscube Estate, Switchback Road, Glasgow, G61 1QH, U.K.

[3] James Watt School of Engineering, University of Glasgow, University Avenue, Glasgow, G12 8QQ, U.K.

[4] IBMC - Instituto de Biologia Molecular e Celular; i3S - Instituto de Investigação e Inovação em Saúde, Universidade do Porto, 4200-135 Porto, Portugal.

[5] School of Molecular Biosciences, Centre for the Cellular Microenvironment, Joseph Black Building, University of Glasgow, University Avenue, Glasgow, G12 8QQ, U.K

[‡] Equally contributing authors

*Corresponding authors: julia.cordero@glasgow.ac.uk and jessica.perochon@glasgow.ac.uk

Keywords: intestinal biomechanics, vascular intestinal stem cell niche, intestinal stem cells, intestinal regeneration, intestinal tumourigenesis, interorgan signaling.

**Abstract**

The vasculature is a prominent component of developmental and adult tissue microenvironments. How, tissue specific characteristics and environmental states influence vascular biology and function, remains largely understudied.

Previously, we discovered crosstalk between the adult intestinal epithelium and the vasculature-like tracheal system of the fruit fly *Drosophila melanogaster*, which is driven by reactive oxygen species (ROS) during pathogen induced-intestinal regeneration. However, chemical stress signals alone are insufficient to explain the rich diversity of vasculature/tissue interactions in living systems and justify the widely observed adaptation of the vascular network in physiology and disease. Here, we uncover reciprocal, mechanochemical interorgan communication between the adult intestine and its vascular niche, which shapes vascular and epithelial tissue adaptations and drives stem cell proliferation during intestinal regeneration and tumour growth. Mechanistically, apoptotic epithelial cells within the regenerating intestine induce local and global mechanical changes in the gut, which results in activation and upregulation of the mechanosensitive ion channel Piezo in a subset of gut-associated trachea. Piezo drives a specific molecular program within the trachea through activation of the mechanosensitive transcription factor Yorkie/YAP, leading to tracheal remodelling and intestinal stem cell proliferation. Furthermore, we identify a non-redundant role of vascular Piezo1 driving remodelling of the intestinal crypt vasculature and inducing crypt growth, WNT signalling activity, and stem cell proliferation in the regenerating mouse small intestine.

Our cross-species *in vivo* study reveals previously unrecognised mechanosensory regulation of intestinal regeneration and tumourigenesis through the vascular-stem cell niche and highlights the importance of studying tissue and context specific vascular cell biology to understand intestinal plasticity and the complexity of tissue/vasculature interactions within a living organ.

## Introduction

The adult intestine is a remarkably plastic organ, capable of responding to a myriad of environmental stimuli through intrinsic cellular adaptations and complex interactions with a highly heterogeneous microenvironment (1-3). Within the intestinal epithelium, intestinal stem cells (ISCs) have a vast regenerative capacity, required to enable a high turnover of the epithelial lining and maintain tissue homeostasis (4-6), while diverse enteroendocrine cell populations endow the intestine with rich sensory and signalling functions (7, 8) and enterocytes contribute to absorptive and metabolic functions of the intestinal epithelium (9, 10). How, specialised interactions between the intestinal epithelium and it's diverse microenvironment contribute to tissue plasticity and the functional versatility of the adult intestine, is poorly understood.

The vasculature interacts with target tissues through the exchange of oxygen, metabolites and angiocrine factors (11-13). Molecular analysis of vascular endothelial cells across tissues, reveals tissue specific characteristics of the vascular microenvironment, likely tailored to individual needs of each target tissue. Beyond supporting organ specific functions, the vascular system of highly self-renewing and plastic tissues, such as the intestine and the skin, must adjust to frequent and often dramatic tissue remodelling processes, which range from discrete cellular adaptations to whole organ resizing, in response to a diverse range of environmental stimuli and organismal states (14-20). The biology underpinning context dependent cellular interactions and adaptations of the vascular microenvironment within an individual tissue remains significantly understudied.

The diversity of interactions between the adult intestine and its vascular microenvironment are reflected in the crosstalk between the midgut and its rich tracheal network in the fruit fly *Drosophila melanogaster* (14-17). The *Drosophila* tracheal system is a mesh-like structure composed of oxygen-delivering tubes, functionally and molecularly alike the mammalian blood vasculature and respiratory system (21, 22). *Drosophila* terminal tracheal cells (TTCs), which are related to vertebrate vascular tip cells (23), extend prominent cytoplasmic projections to supply oxygen to their target tissues (21, 24, 25). Previous work from us and others showed a crosstalk between the intestinal epithelium and the vasculature like

tracheal tissue in *Drosophila* during pathogen-induced intestinal regeneration and tumour growth triggered by ROS dependent signalling (14, 15). However, chemical stress signals alone are insufficient to explain the broad tracheal/midgut interactions observed in the adult fly midgut (14, 15, 17) or adaptation of the mammalian vascular network in broad physiological settings (18-20).

Through *in vivo* genetic studies in flies and mice, combined with live imaging, quantitative biology and biophysical approaches, we reveal previously unrecognised mechanosensory regulation of intestinal regeneration and tumorigenesis through the vascular- intestinal stem cell niche and present the first report on the role of the blood vasculature and vascular expressed Piezo1 as functional contributors to crypt regeneration in the adult mouse small intestine.

## Results

### Cellular and tissue-scale re-sizing of the regenerating intestine correlate with remodelling of associated tracheal/vascular tissue.

The adult *Drosophila melanogaster* gut is densely surrounded by TTCs, which we labelled with *GFP* driven under the control of the Serum Response Factor promoter (*dSRF>GFP*) (14, 15). Remodelling of the adult gut tracheal network in *Drosophila* is regulated through cross-tissue chemical signalling downstream of ROS, which are a prominent feature of midguts subjected to damage by oral pathogenic infection or oxidative stress (14, 15) (Fig. 1a, a' and Extended data Fig.1a, b). However, the presence of ROS is not significant in midguts exposed to the basal membrane disruptor dextran sodium sulphate (DSS)(Extended data Fig. 1c, d) (26), which equally depend on active tracheal remodelling for their regeneration (14) (Fig. 1b, b'). Furthermore, treating flies with the antioxidant N-acetyl cysteine (NAC) alongside DSS has no significant impact on DSS induced tracheal remodelling or ISC proliferation (Extended data Fig. 1e-g). Such observations suggested that, remodelling of the adult gut associated trachea, is a response to diverse cues working cooperatively or independently from oxidative stress signals. Understanding such alternative processes of gut/tracheal interactions might explain the aetiology of organ associated vascular remodelling observed in broad physiological and pathological settings (18-20, 27-30).

Organ resizing are poorly understood phenomenology associated with adult midgut regeneration in *Drosophila* (14, 31). Image segmentation and quantitative morphometric analysis of control and damaged midguts revealed increased thickness of the dorsal-ventral (D/V) axis and/or shortening of the anterior-posterior (A/P) length in posterior midguts during *Pe* or DSS treatment (Fig. 1c-h). Next, we used available tools for image segmentation and morphometric analysis (32) to quantify cellular morphology parameters within the midgut epithelium from masks of segmented enterocytes (EC), which represent approximately 80% of the midgut epithelium. We observed a significant increase in eccentricity— a deviation from cellular circularity associated with mechanical changes (33, 34)— in ECs from *Pe* (Fig. 1i-j) or DSS treated midguts (Fig. 1k-l).

Next, we asked whether only introducing a mechanical stimulus to the intestinal epithelium would be sufficient to induce the tissue and cellular resizing as well as the tracheal remodelling observed in regenerating midguts. To address this, we fed flies with an indigestible fibre, methylcellulose, previously shown to induce an 'overfull' phenotype in the gut (35). We observed that methylcellulose feeding in the absence of damage recapitulated all morphological changes of regenerating midguts, including shortening of the A/P length of the gut tube, thickening of the D/V axis, and increased EC eccentricity (Fig. 1m-q). Importantly, gut morphological changes in methylcellulose fed animals were accompanied by a significant increase in remodelling of midgut associate terminal tracheal cells (TTCs) (Fig. 1r, s).

Finally, we measured cell morphology in control and regenerating crypts of the mouse small intestine, following 72 hrs post-injury by whole body irradiation (IR), which represents the point of maximal regenerative proliferation in the small intestinal crypts (36). We used immunostaining for E-cadherin to segment crypt cells for morphological analysis (Fig. 1t), which revealed a significant increase in cellular eccentricity of crypts from irradiated versus untreated mice (Fig. 1t', u). Observations reported in our previous study indicated an increase in CD31+ endothelial cells surrounding regenerative crypts of the mouse small intestine (14). A refined assessment of the blood vasculature through whole mount tissue preparations and immune-detection of Pecam-1, a marker of blood vascular endothelial cells, confirmed increased branching of crypt blood vasculature in the regenerating mouse small intestine (Fig. 1v, w). Therefore, as in the *Drosophila* midgut, changes in intestinal epithelial cell morphology correlate with increased remodelling of the blood vasculature surrounding regenerating crypts of the mouse small intestine.

Altogether these results suggest that mechanical changes of the intestinal epithelium are prominent and consistent features across regenerating intestinal models, which co-exist with ROS in a pathogen induced model of midgut regeneration. Furthermore, mechanical forces in the absence of intestinal damage are sufficient to drive remodelling of the midgut associated tracheal network.

**The midgut epithelium experiences regionalised mechanical forces during intestinal regeneration.**

While cell morphological changes are indicative of mechanical stress, further information is necessary to quantify mechanical forces within a tissue. Prior studies have compartmentalised the adult fly gut into histologically, molecularly and metabolically defined sub-regions (37, 38) (Fig. 2a). Despite the global nature of the gut epithelial damage used in our models of intestinal regeneration, phenotypes of tracheal remodelling and EC cell changes were regionalised across the posterior midgut. We observed that, while tracheal remodelling and EC aspect ratio were significantly increased in the R4 of the posterior midgut from *Pe* fed animals, both parameters remained largely stable in the R5 segment (Fig. 2b-e). Therefore, we took advantage of this phenomenology to more directly correlate changes in local intestinal mechanics with tracheal remodelling within individual midguts. First, we used an available Bayesian Force Inference model in MATLAB to predict relative forces in the midgut tissue across the R4 and R5 regions from tile scan images of *Pe* infected and control guts, using the R5 gut region as internal control. We observed a significant increase in cell pressure in the R4 region relative to R5 upon infection, which was not observed in homeostasis (Fig. 2f-g'). To directly quantify regional mechanical properties in the midgut, we next used nanoindentation to measure stiffness of the gut tube across the R4 and R5 regions of freshly dissected control and orally infected midguts (Fig. 2h). We detected a significant increase in stiffness specific to the R4 region of the gut upon infection (Fig. 2i), which correlates with the increased tensional state of this midgut region as evaluated from the force inference analysis. Altogether, these results provide novel quantitative and qualitative data correlating biomechanics of the intestinal epithelium and whole midgut with remodelling of the tracheal gut microenvironment.

**Midgut enterocytes and gut associated tracheal cells establish physical contact during intestinal regeneration**

Cellular projections of TTCs appear located between the visceral muscle layer of the gut and the midgut epithelium (14). We reasoned that one way for trachea to sense morphological changes within the midgut epithelium would be through direct physical contact with ECs. To test this, we used the GRASP (GFP reconstitution across synaptic partners) system (39) to visualise points of close proximity between tracheal cells and ECs by expressing the 11$^{th}$ strand of a split GFP in the main tracheal branches under a *Btl-lexA* driver and strands 1-10 in ECs under the *Mex-*

*Gal4* driver (Fig. 2j). While a constitutive red signal will allow visualisation of gut associated trachea (Fig. 2j), a GFP signal would only be detected upon close interaction between tracheal cells and ECs. While in homeostatic conditions we saw RFP but little GFP reconstitution, *Pe* infected midguts revealed the expected increased tracheal branching and a significant increase in the number of GFP positive enterocytes within the epithelium (Fig. 2k, l). We observed no GFP signal in midguts independently expressing individual GRASP components (Fig. 2m, n). These results suggest the presence of physical interaction between ECs and gut associated trachea, which are induced during midgut regeneration. As such, gut-associated tracheal cells may be equipped to directly sense mechanical changes within the intestinal epithelium.

**Enterocyte apoptosis is necessary and sufficient to influence the biomechanical properties of the intestine and gut associated tracheal remodelling.**

Imbalance between cell proliferation and cell loss within the *Drosophila* midgut epithelium has been associated with major organ resizing (31, 40). Our previous light microscopy analysis of adult midgut associated trachea suggested that EC cell death rather than ISC proliferation determines tracheal cell remodelling (14). Here, we used a dual driver genetic system to induce adult EC cell death by overexpressing the pro-apoptotic gene *bax* (*Mex$^{ts}$>bax*) while fluorescently labelling the tracheal system, with a previously characterised tracheal specific *QF/QUAS* line (*QF6>mtd-Tomato*) (15). Using this approach, we confirmed that EC death in the absence of external damaging cues is sufficient to induce tracheal remodelling (Fig. 3a, b). We therefore hypothesised that cell death could be driving morphological and mechanical changes in the midgut epithelium, leading to tracheal remodelling.

Firstly, we observed a significant increase in cellular eccentricity in the posterior midgut epithelium, following a short pulse of global Bax overexpression within ECs from the undamaged midgut (Fig. 3c-d). To refine our analysis of EC apoptosis into a localised rather than global setting, we next performed a time course of oral *Pe* infection to monitor the earliest appearance of discrete cell death using a live apoptotic sensor (41). We observe areas with individual apoptotic ECs 2hs after initiation of *Pe* feeding (Fig. 3e; GFP$^{+ve}$; arrow). Segmentation and morphometric

analysis revealed a localized pocket of epithelia with increased cellular eccentricity restricted to the area immediately surrounding an individual apoptotic cell (Fig. 3e'-f). Lastly, blocking EC apoptosis by overexpressing the apoptotic inhibitor, p35 (*Mex*$^{ts}$*>p35*) significantly reduced cellular eccentricity (Fig 3g-h) and decreased gut stiffness upon *Pe* infection (Fig. 3i). Importantly, while EC p35 overexpression inhibited damage induced tracheal remodelling (Fig. 3j, k), it did not affect ROS levels in *Pe* infected midguts (Fig. 3l, m). This set of data suggests that EC cell death is a determinant factor in the morphological and biomechanical changes quantified in regenerating intestines.

**Mechanical changes within the intestine are sensed by tracheal mechanosensory channel Piezo**

The mammalian vasculature is a highly mechanosensitive tissue. Stimulation of vascular endothelial cells by intrinsic shear stress and stiffness are capable of driving angiogenesis and vascular remodelling (42-44). Mechanical signals within the vascular endothelium are largely transduced through TRP and Piezo family ion channels (45, 46). While the role of Piezo1 in vascular development is well documented (47), little is known about mechanisms of regulation and/or function of vascular Piezo1 in adult self-renewing epithelia.

Recent studies in adult *Drosophila* and mouse intestine reported a role of stem/progenitor cell expressed Piezo in homeostatic stem cell maintenance and differentiation of the secretory lineage of intestinal stem cells (35, 48). While a single *piezo* gene exists in *Drosophila* (49), described functions of *Piezo* within the mammalian intestinal epithelium, are redundant between *Piezo1* and *Piezo2* (48).

Given the physical interaction observed between midgut ECs and tracheal cells (Fig. 2j-l), we hypothesised that, changes in the mechanical properties of the regenerating midgut epithelium, could be detected through mechanosensory channels expressed in the gut associated tracheal tissue. Using an available *GAL4* reporter of endogenous *piezo* gene expression *(piezo-GAL4)* (35) we identified subpopulations of tracheal cells expressing *piezo* in the adult posterior midgut (Fig.4a). Strikingly, we observed a significant increase in tracheal *piezo* expression upon intestinal damage with orally administered *Pe* or DSS (Fig. 4a, b). Tracheal

*piezo* upregulation was confirmed with a reporter of Piezo protein expression Piezo$^{mimic}$ (Extended data Fig. 2a, b) (50, 51). Consistent with previous reports (14, 15), general tracheal remodelling of *Pe* treated midguts was significantly reduced upon neutralization of ROS with NAC treatment (Extended data Fig. 2c). However, *piezo* upregulation within trachea of *Pe* treated midguts was not dependent on oxidative stress (Extended data Fig. 2d, e). However, we noted that *piezo* expressing TTCs showed partially reduced remodelling following *Pe* treatment (Extended data Fig. 2d), suggesting that some of the mechanisms leading to tracheal remodelling downstream of *piezo* may be shared with those activated by oxidative stress (14, 15). Methylcellulose induced mechanical stretch of the intestine in the absence of damage, recapitulated *piezo* upregulation in TTCs (Extended data Fig. 2f, g). Selective chemical activation of Piezo by agonist Yoda1 was sufficient to induce upregulation of *piezo* expression within the trachea, tracheal remodelling and ISC proliferation (Fig. 4c-f and Extended data Fig. 2h). Overall, these results indicate that mechanical changes within the regenerating *Drosophila* midgut epithelium lead to non- autonomous upregulation of *piezo* in a subpopulation of gut associated trachea. Remarkably, Piezo activation upregulates *piezo* gene expression within adult *Drosophila* midgut trachea (Fig. 4c, d).

Next, we used RNA interference gene knockdown to assess the functional role of tracheal *piezo* in TTC remodelling and ISC proliferation in regenerating midguts. Our results showed that, knocking down *piezo* in adult TTCs (*dSRF$^{ts}$>piezo-IR*), impaired tracheal remodelling and ISC proliferation upon midgut epithelium injury through oral administration of *Pe* or DSS (Fig. 4g-i). However, epithelial eccentricity was not affected in *dSRF$^{ts}$>piezo-IR* midguts (Extended data Fig. 2i, j), suggesting that mechanical changes of the midgut epithelium precede tracheal *piezo* activation and function in midgut regeneration. Additionally, overexpression of tracheal *piezo* upon infection significantly potentiated tracheal remodelling and ISC proliferation during midgut regeneration and impaired the recovery of tracheal and ISC homeostasis following removal of damage (Fig. 4j-l). Therefore, tracheal *piezo* is necessary and sufficient for remodelling of gut associated TTCs and it is an instrumental regulator of intestinal regeneration dynamics during and post-damage.

**Dynamic *piezo* regulation and activity during damage induced midgut regeneration.**

To further characterize *piezo* expression in the midgut, we performed a time course experiment, which revealed a gradual increase in gut-associated tracheal *piezo* expression during a 16h period of *Pe* feeding (Fig. 4m, n). The observed time-dependent pattern of *piezo* expression correlated with gut tracheal remodelling dynamics and nanoindentation measures of intestinal tube stiffness (Fig. 4o, p).

Signalling downstream of Piezo channel activity involves the increase of intracellular Calcium ($Ca^{2+}$) influx (46, 47). We therefore used a genetic $Ca^{2+}$ sensor (*GCamp7s*) expressed in tracheal cells to measure Piezo activity during a time course of intestinal damage (Fig. 4q). Intracellular $Ca^{2+}$ levels in TTCs depicted a temporal pattern of increase consistent with the one established for tracheal remodelling and *piezo* expression during the monitored stages of midgut damage (Fig. 4q, r). Importantly, we confirmed that *GCamp7s* activation in gut associated trachea was dependent on Piezo (Extended data Fig. 2k, Supplementary Movies 1-3). Furthermore, longitudinal studies through in vivo imaging allowed us to visualise discrete $Ca^{2+}$ pulses in extending and fusing cytoplasmic projections of TTCs as early as 2hs after the start of *Pe* feeding (Fig. 4s). This timeframe precedes a detectable increase in global tracheal remodelling (Fig. 4m).

In summary, this set of results suggests that temporal patterns of *piezo* gene upregulation and Piezo channel activation in gut associated trachea overlap with the dynamic of gut trachea remodelling and gut biomechanical changes observed during midgut regeneration. Importantly, our *in vivo* tracking of $Ca^{2+}$ influx in tracheal cells suggest that Piezo activation in gut associated trachea precedes a global increase in tracheal remodelling.

**Piezo activates a Yorkie/YAP-TAZ dependent mechanosensory program for tracheal remodelling in the regenerating midgut.**

We next looked into the downstream mediators of the role of Piezo in midgut tracheal remodelling, by first assessing its impact on an oxidative stress responsive tracheal programme, including regulation of Fibroblast growth factor-like *branchless*

(*bnl*) and its receptor breathless (*btl*) in TTCs (14, 15). Interestingly, while *piezo* knockdown from trachea impaired Bnl upregulation following oral *Pe* infection (Fig. 5a, b), it did not affect upregulation of the gene encoding for the Bnl receptor, *btl* (Extended data Fig. 3a, b). On the other hand, *piezo* knockdown led to significant decrease in Myc expression in TTCs (Fig. 5c, d), which is also a target of oxidative stress signals (14, 15). These results suggest that mechanical and oxidative stress signals partially overlap in the molecular programs they regulate in midgut associated trachea during midgut regeneration.

How does Piezo activation lead to transcriptional changes in TTCs? We hypothesise that the mechanosensitive transcription factors YAP/TAZ, which have been functionally linked to Piezo 1 in mammalian endothelial cells (52-54), may mediate the transcriptional effects of tracheal Piezo during midgut regeneration. *Drosophila* Yorkie (Yki) is the orthologue of mammalian YAP/TAZ. As with their mammalian counterparts, Yki activation following cell intrinsic or extrinsic mechanical cues leads to its translocation from the cytoplasm to the nucleus to drive transcriptional target regulation. Using an endogenous Yki protein reporter line, we monitored Yki localisation within gut associated trachea in homeostatic and regenerating midguts. In homeostasis, Yki expression was largely restricted to the cytoplasm of TTCs, however, upon pathogenic infection or DSS feeding we saw significant translocation of Yki to TTCs nuclei (Fig. 5e-g). Importantly, *piezo* knockdown inhibited translocation of Yki in TTCs form regenerating midguts (Fig. 5e-g). Therefore, Yki is activated in remodelling trachea from the regenerating midgut in a Piezo dependent manner.

We next assessed the functional role of tracheal Yki in TTC remodelling and regenerative ISC proliferation in the adult midgut. Knocking down *yki* from the adult trachea using two independent RNAi lines resulted in a significant decrease in TTC remodelling and ISC proliferation in *Pe* infected midguts (Fig. 6a-c). Conversely, overexpression of a constitutively active Yki in adult TTCs potentiated tracheal remodelling during the damage phase of intestinal regeneration and delayed homeostasis recovery of both TTC remodelling and ISC proliferation even 48hs after removing flies from pathogen containing food (Fig. 6d-f). Finally, to further interrogate the functional link between Piezo and Yki in midgut associated trachea, we assessed a potential dependency on Yki for Bnl and Myc upregulation in TTCs from

regenerating midguts. Consistently with the interrelationship observed between Piezo and Yki (Fig. 5e, g), tracheal *yki* knockdown lead to significant impairment in both, Bnl and Myc upregulation in TTCs from regenerating midguts (Fig. 6g-j).

Our results reveal a mechanosensitive model of gut/tracheal interaction during adult midgut regeneration where Piezo activation and upregulation within gut associated trachea is translated into a cell intrinsic molecular program through the activation of Yki in terminal tracheal cells, leading to regenerative tracheal remodelling and ISC proliferation (Fig. 6k)

**The blood vasculature and vascular Piezo 1 are functional components of the regenerative stem cell niche in the mammalian small intestine.**

The rich microenvironment of the mammalian gastrointestinal tract is composed of diverse cellular subtypes, including multiple mesenchymal cell populations, enteric neurons, and endothelial cells that together provide physical support, contractility, and multiple stem cell niche factors to the adult intestinal epithelium (55-61). While lymphatic vessels are known as functional components of the mammalian stem cell niche, supporting intestinal stem cell function during tissue homeostasis and regeneration (55, 62), the role of the intestinal blood vasculature remains unknown.

Using single molecule RNA in situ hybridisation, we detected co-expression of *Piezo1 and* vascular *Pecam-1* in the mouse small intestinal crypt (Fig. 7a). We used a tamoxifen inducible *Pdgf-β-Cre-GFP* (63) for visualisation of the intestinal blood vasculature from whole mount tissue preparations (Fig. 7b) (64) and to investigate the role of the blood vessels and vascular Piezo1 in the mouse intestine. We used control *Pdgf-β-CreER-GFP* mice (*Piezo 1*$^{wt/wt}$) or *Pdgf-β-CreER-GFP* mice combined with an inducible Piezo1 knockout allele (*Piezo 1*$^{fl/fl}$) to knock out *Piezo1* from the adult blood vasculature. Adult mice were treated with tamoxifen for Cre activation and allowed to age for 5 days prior to induction of intestinal damage by 10 Gy whole body irradiation (IR), followed by sampling at 72 hours post IR (Extended data Fig. 4a).

Strikingly, knocking out *Piezo1* from the adult vasculature had no impact on homeostatic intestinal vascular remodelling (Extended data Fig 4b-d) or self-renewal of the intestinal epithelium (Fig. 7c-e and Extended data Fig. 4 e-h). However,

vascular *Piezo1* knock out animals showed a significant impairment in crypt vascular remodelling (Fig. 7f, g), and a decrease in the total number of regenerating crypts and proliferating cell within intestinal crypts following irradiation-induced damage (Fig. 7h-j). Furthermore, Wnt signalling activity as per levels of Myc and Sox9 (65, 66) in post-damage regenerating crypts was impaired in *Piezo*$^{fl/fl}$ mice compared to *Piezo*$^{wt/wt}$ counterparts (Fig7k-m). Therefore, while dispensable to adult intestinal and intestinal vasculature homeostasis, endothelial Piezo1 is necessary for vascular remodelling and intestinal cell proliferation within regenerating crypts of the mouse small intestine, following irradiation induced damage.

**Piezo drives tracheal remodelling and intestinal hyperplasia in a *Drosophila* model of intestinal tumourigenesis.**

Previous work reported active remodelling and a functional role of gut associated trachea in fly models of oncogenic *ras* and *Notch* driven tumourigenesis (15). Hyperplasia of the adult intestinal midgut epithelium induced through stem cell overexpression of the *Src* oncogene (*esg*$^{ts}$*>Src*), leads to adenoma like structures, which are likely to cause mechanical stress within the intestinal epithelium (67). Consistently, *esg*$^{ts}$*>Src* midguts showed whole tissue and cellular morphology changes akin to those observed in damaged or methylcellulose treated midguts (Fig. 7n-r). We generated a new transgenic system for Src overexpression (*lexAop-Src*) to allow independent genetic labelling and manipulation of tracheal cells combined with intestinal stem cell induction of *Src* overexpression. We confirmed the presence of intestinal stem cell hyperproliferation and increased tracheogenesis in *esg*$^{ts}$*-LexA/LexAop-Src* midguts (Extended data Fig. 4i-k). Furthermore, a Piezo protein reporter fly line, revealed significant increase in tracheal Piezo expression following Src overexpression in the intestinal epithelium (Fig. 7s, t). Importantly, knocking down *piezo* in TTCs, inhibited tracheal remodelling and intestinal hyperplasia in Src overexpressing midguts (Fig. 7u-w). Therefore, we show that tracheal Piezo is also necessary for tumour induced tracheal remodelling and the reciprocal action of the trachea in intestinal tumorigenesis in *Drosophila*.

Altogether, our cross-species study reports a novel pro-angiogenic mechanical crosstalk between the intestinal epithelium and the tracheal/vascular tissue. Mechanical forces generated by apoptotic intestinal epithelial cells during

intestinal regeneration contribute to cellular and tissue resizing and mechanical changes within the intestinal epithelium, which induce activation of a subset of trachea/vascular cells expressing the mechanosensory channel Piezo. Piezo activation in the vascular microenvironment is necessary and sufficient to drive remodelling of the vascular niche and intestinal stem cell proliferation during regeneration and tumourigenesis.

## Discussion

The vasculature is as an intrinsically mechanosensitive tissue and an important constituent of the microenvironment of developing and adult organs. Whether and how those vascular characteristics converge during the support of target tissues is not well understood.

A few of the many diverse contexts of vascular remodelling in physiology and disease include pregnancy and foetal growth, wound healing, bone fracture repair, tumour growth and metastasis (20, 30, 68-72). A seemingly common theme amongst the mentioned examples is the presence of vascular adaptation to environmental and/or host organ changes. In contrast to the vast number of studies on intrinsic forces driving vascularization, such as fluid shear stress (73), the impact and identity of extrinsic physical cues on angiogenesis and vascular remodelling remains largely understudied. Here, we report a novel cross-species pro-angiogenic mechanical crosstalk between the intestinal epithelium and the tracheal/vascular system, which drives reciprocal adaptation of the intestine and vascular microenvironment during intestinal regeneration and tumorigenesis.

### A diversity of extrinsic signals leading to common phenomenology of post-developmental vascular remodelling

Hypoxia and oxidative stress modulate vascular/tracheal remodelling across species (74-77). Nevertheless, adaptive vascularization of adult organs is observed in the context of a wide range of chemical, physiological and environmental cues (14-20, 78).

Our previous observations showed a conserved phenomenology of tracheal/vasculature changes upon diverse intestinal insults (14). Here, we demonstrate that mechanical forces from the intestinal epithelium are a common denominator in gut/tracheal interactions during intestinal regeneration and tumorigenesis. As such, our new findings may explain mechanisms of vascular remodelling observed in board physiological and pathological contexts.

What underpins the diversity of vascular/tracheal adaptations across and within tissues? Our results revealed Piezo expression in a subpopulation of gut associated trachea (Fig. 4), which do not appear to depend on FGFR/Btl for their function (Extended data Fig. 3). Furthermore, while *btl* expression is dependent on ROS (14), *piezo* expression is largely refractory to the action of the antioxidant NAC (Extended data Fig. 2). These results suggest that TTCs in the adult intestine may be highly heterogenous. For instance, Piezo and Btl expressing trachea could represent two distinct sub-populations. Tracheal cell diversity may explain the ability of the tracheal/vascular microenvironment to respond to different cues and support intestinal function accordingly.

Despite the heterogeneous nature of *piezo* expression in midgut trachea, gene knock down from TTCs results in rather global effect on tracheal remodelling (Fig. 4). A similar phenomenon is observed upon *btl* knockdown (14, 15). How do context specific cues sensed by a sub-set of tracheal cells translate into global vascular/tracheal responses? One possible answer to this open question may lie in the existence of paracrine interaction amongst distinct tracheal cell populations. While definite proof of such a phenomenon remains to be obtained, our live imaging visualization of intracellular $Ca^{2+}$ signals in gut-associated trachea revealed the presence of branch fusion events between distinct tracheal cells and transfer of intracellular calcium, during TTC remodelling (Fig. 4).

**Cellular apoptosis as a regulator of intestinal biomechanics and gut associated tracheal remodelling during intestinal regeneration.**

Here, we show enterocyte morphology and mechanical changes within the intestine are conserved across different challenges, including chemical and pathogenic damage, physical forces and tumour formation (Figs.1 and 7). Whilst the intestinal visceral muscle and the extracellular matrix likely contribute to the

biomechanical properties of the gut, intestinal epithelial changes appear to be a predominant determinant of cellular and tissue mechanical properties measured in regenerating midguts (Figs. 1-3).

We identified physical interaction between trachea and intestinal EC and EC apoptosis as an important cue driving mechanical changes in regenerating midguts as well as tracheal remodelling. Previous studies have characterized a force generating role of cell death in developmental and homeostatic contexts. Apoptosis influences shape and size of developing tissues (79, 80). Furthermore, in a phenomenology reminiscent to our observations on individual apoptotic cells (Fig.3), cells closest to apoptotic cells experience tensile stretching in a model of homeostatic compensatory proliferation *in vitro* (81). Our findings suggest that proposed roles of apoptosis in tissue biomechanics may also apply to a complex, multilayer epithelial tissue such as intestine. However, apoptosis is likely a context dependent rather than universal driver of biomechanical organ/vascular interactions.

Tumorigenesis is associated with significant mechanical changes such as increased tissue stiffness (44). The non-receptor tyrosine kinase Src is activated within the intestinal epithelium in response to mechanical cues from the mesenchymal microenvironment (82). Consistently, intestinal tumours overexpressing Src induce midgut tracheal remodelling in a Piezo dependent manner (Fig. 7). The role of apoptosis in tumour-induced mechanical changes in the intestine and gut associated trachea, remains to be addressed.

**Multicellular role of Piezo mechanosensing in the adult intestine**

Pioneering work in *Drosophila* discovered a cell autonomous role of Piezo within stem/progenitor cells in the intestine, during differentiation of the secretory lineage of ISCs (35). Similarly, subsequent work in the mammalian intestine reported redundant roles of intestinal stem cell Piezo1 and Piezo2 in homeostatic stem cell maintenance and differentiation of secretory cell lineages in the intestine (48).

Using *Drosophila* and mouse models, our results demonstrate a distinct and non-redundant role of vascular/tracheal Piezo1 in intestinal regeneration, contributing to angiogenesis and ISC proliferation during intestinal regeneration and tumorigenesis. Whilst we show that vascular *Piezo1* is necessary for damage induced stem cell proliferation and crypt regeneration in the mouse small intestine,

Its impairment does not impact homeostatic vascular remodelling or self-renewal of the intestinal epithelium (Fig. 7). Furthermore, we observed no significant impact in secretory lineage differentiation in either homeostatic or regenerating intestines following *Piezo1* knockout from the adult vasculature.

As such, our *in vivo* work reports a novel function for Piezo1 in the intestine and suggests an exciting therapeutic opportunity to target Piezo1 for regenerative and anti-tumour purposes with low impact on basal tissue homeostasis.

## Materials and Methods

### Fly stocks and husbandry.

A list of the fly and mouse lines and full genotypes of animals used in this study can be found in a dedicated section of the Materials and Methods. For temperature sensitive experiments, using the *GAL4/UAS* or *LexA/LexAop; GAL80$^{ts}$* system, flies were crossed, the $F_1$ progeny were reared, and experimental adults were aged for 3-5 days after eclosion at 18°C. Then, animals were moved to 29°C for 5 days to allow transgenes activation. Experiments that did not involve temperature-sensitive transgenes were performed with animals kept at 25°C and experimental adults aged for 5 days prior to any procedure. All experimental animals were transferred to fresh food every 2 days. Only posterior midguts from adult mated females were used in this study.

<u>Generation of *lexAop-Src* transgenic line</u>: Genomic DNA from *UAS-Src* flies (67) was extracted and used as a template to amplify the inserted *Src* sequence by PCR using the following vector specific primers: *AGATCTGCGGCCGCATCCTCTAGAGTCGATCGACAT* (forward), *AGGTACCCTCGAGCCTGCAGGCATGCAAGCTT* (reverse). The resulting PCR product was purified and cloned into NotI-XhoI sites of *pJFRC19* (Cat No 26224; Addgene) to generate *pJFRC19-Src*. Following *pJFRC19-Src* sequence confirmation, the transgene-containing plasmid was injected for the generation of *13xLexAop-Src* flies by BestGene Inc.

### *Drosophila* intestinal damage models.

*Bacterial infection* - *Pseudomonas entomophila* (*Pe*) – females were fed on filter papers containing a 5% sucrose solution only or sucrose containing *Pe* $OD_{600}$=100 for 16h.

*DSS treatment* - (Sigma-Aldrich, cat no. 42867) – females were fed on filter papers containing a 5% sucrose solution only or sucrose containing 3% DSS for 2 days with fresh medium applied daily.

*Methylcellulose feeding* - (Sigma-Aldrich, cat no. 274429) – females were fed on normal food as a control or on sucrose food containing 10% methylcellulose for 72h. Flies were transferred onto new food every two days. Prior to dissection, control flies were transferred over night to 5% sucrose on filter papers to clear the gut. Flies exhibiting guts with over a 50% increase in diameter were selected as exhibiting the 'full gut' methylcellulose phenotype.

***Drosophila* chemical treatments.**

*NAC treatment* - (Sigma-Aldrich, cat no. A7250) – Flies were placed on filter paper discs soaked with a 5% sucrose solution containing 20mM NAC for 24h. Then, the animals were fed with either 5% sucrose + NAC or 5% sucrose + NAC + *Pe* ($OD_{600}$=100) for 16hs or 5% sucrose + NAC + 3% DSS for 48hs.

*DHE treatment* - (Invitrogen Molecular Probes, cat no. D23107) – Tissues were dissected in Schneiders medium and then incubated in 30mM DHE solution for 5-7mins at room temperature and in a dark chamber. Then, midguts were washed three times with Schneiders medium for 5min, mounted in DAPI containing media followed by immediate imaging and image capture.

*Yoda1 treatment* – Yoda1 (Tocris, cat no. 5586) was suspended in DMSO and diluted to 1 µM in 5% sucrose. Vehicle containing an equivalent volume of DMSO in 5% sucrose was used as control. Flies were placed in vials containing filter paper discs soaked with either solution for 16h at 29°C prior to dissection.

***Drosophila* immunohistochemistry.**

Guts from adult female flies were dissected in PBS and immediately fixed in 4% formaldehyde (FA, EM grade, Polysciences) diluted in PBS for 1h at room temperature (RT) and then washed three times in PBS-T (PBS + 0.2% Triton X100). Samples were incubated with the primary antibody diluted in PBT (PBS-T + 2 % BSA)

overnight at 4°C. Guts were washed three times in PBS-T and then incubated with secondary antibody in PBT for 2h at RT. After incubation, guts were washed three times for 20min in PBS-T and mounted on glass slides with 13mm x 0.12mm spacers (sigma) in Vectashield mounting medium with DAPI (Vector Laboratories). For anti-Myc, anti-β-gal and anti-Bnl staining, fixation was performed in 4% formaldehyde for 1h, followed by 5min methanol fixation added to the sample gradually and then 10min in 100% methanol. Samples were blocked in 7% goat serum for 1h before primary antibody incubation. The following primary antibodies were used: chicken anti-GFP (1:200, Abcam, cat. no. ab13970), rabbit anti-DsRed (1:1000, Clontech, cat no. 632496), mouse anti-Dlg (1:50, DSHB 4F3E2, AB 528203), mouse anti-PH3 (1:100; Cell Signaling, cat. No. 9706), rabbit anti-β-gal (1:1,000; MP Biochemicals, cat no. 559761), guinea pig anti-Myc (1:100, gift from G. Morata), rat anti-Bnl (1:50, M. Krasnow. Secondary antibodies: Alexa Fluor anti-chicken 488 (1;200), anti-rabbit 594 (1:100) and anti-mouse 647 (1:100) (Invitrogen) were used. Guts were mounted in Vectashield anti-fade mounting medium for fluorescence with DAPI (Vector Laboratories, Inc.) to visualize all nuclei.

**Image acquisition.**

Confocal Microscopy (Zeiss LSM 780/880) – Each image represents half-volume of the posterior midgut (area between hindgut and the copper cell region) and was acquired with a ×20, ×40 or ×63 lens on a Zeiss LSM 780 or 880 confocal microscope using identical acquisition conditions for all samples from a given experiment. The images represent the maximal intensity projection of Z-stacks and were processed using ImageJ (Version 1.54f) and Carl Zeiss Zen 3.0 to adjust the brightness and contrast.

Nanoindentation – Flies were anesthetised on ice and midguts were freshly dissected on the day of measurement in Schneider's *Drosophila* medium (1x Sigma Aldrich 50146) and then transferred onto a 0.28 mg/ml Cell-Tak (Corning, 354240) pretreated glass bottom petri dish (thickness 1,5) with Shneider's *Drosophila* medium for tissue hydration. Petri dishes were coated with 10µl of Cell-Tak overnight followed by 2 washes with PBS and air drying. A Chiaro nanoindentation device (Optics11, The Netherlands) integrated above an inverted Zeiss Axiovert 200M microscope was used to probe gut mechanics using a procedure previously described (83). A

cantilever (stiffness ($K$)= 0.52 $Nm^{-1}$) with a spherical tip (radius= 3.0-3.5 µm) was used to probe the midguts *ex vivo*. After probe calibration, an initial indentation was performed to tune the experimental parameters. The threshold, amount of cantilever bending required to recognise a substrate, and find surface values, distance in µm the probe moves after indentation for subsequent indentation, were tuned according to the initial force displacement curve produced. A matrix scan was configured at 25 points per scan at intervals of 5µm along the specified midgut region, scans were repeated twice per region of interest for every midgut. The midguts were approached at 5 µm/s and indented with displacement as defined in the displacement control mode.

*Ex vivo* live imaging – Flies were placed in vials containing filter paper discs with either 400 µl *Pe* or sucrose for 6 hours prior to imaging. Coverslips were glued into imaging mounts and 10 µl Imaging Agarose (Low gelling temperature agarose 6% (Sigma, A4018), Schneider Insect medium (Thermo, 21720024)) was placed on the surface of the coverslip. Flies were dissected in cold imaging medium (Schneider Insect medium (Sigma, 50146), 5% Fly Extract (VDRC), 1:1000 penicillin-streptomycin (Invitrogen, 15140), 10% FBS (Sigma, F4135) and placed on the agarose in modified Schneider's medium as previously described (84). Plates were sealed with lids containing damp paper to maintain humidity. Z stacks of the gut were acquired at a ZEISS 780 in a time series at a rate of 1 stack every 5 minutes for 10 hours unless otherwise indicated.

*In vivo* live imaging – Flies were placed on Pe or sucrose solution for two hours prior to imaging. Flies were glued on their dorsal side and the A1 segment of abdominal cuticle removed. A small portion of the R4 region was gently exposed with forceps and covered with 2 percent low gelling temperature agarose (Sigma, A4018) in Schneider's Insect Medium (Sigma 50146). The dorsal side of the fly was then covered with Imaging medium (Schneider Insect Medium, 5 percent Fly Extract (VDRC), 0.1 percent Penicillin-Streptomycin (Invitrogen, 15140), 10 percent FBS (Sigma F4135)). A coverslip was gently placed over the dorsal side of the fly before imaging on a Zeiss 880 confocal microscope. Acquisitions were taken at 5-minute intervals. Protocol adapted from (85).

**Quantification Methods.**

A/P and D/V length – Gut dorsal-ventral (DV) and anterior-posterior length (AP) were quantified using ImageJ (Version 1.54f) software. Length was measured using the freehand tool in the A/P axis of the posterior midgut. The D/V axis was measured from the widest point of the R4 region.

ISC proliferation - Proliferating cells were detected by immunostaining against PH3. Olympus BX51fluorescence microscope was used to manually, on visual inspection, count the number of cells positive for PH3 staining per posterior midgut.

Tracheal coverage – detailed protocol described in (14). In brief, tracheal tile scans were Z projected in ImageJ (Version 1.54f) and binarised from thresholding. A skeleton was then produced of the R4 and R5 regions of the gut and mean grey value was used to measure coverage of tracheal branches.

ROS fluorescence – For quantification of total ROS levels, pixel intensities of Z stacks (sum slices) were used. The mean of the summed DHE intensities averaged from each tissue was used for statistical analysis.

Eccentricity - Images of the intestinal epithelium were projected using the local z projector plugin in ImageJ (Version 1.54f) to produce a curvature corrected Z projection and heightmap. Z projected images were then segmented in cellpose. Cellpose segmentations were converted to 4-bit connectivity images using an ImageJ plugin morpholibJ to create a cell mask (32). Masks and heightmaps from each sample were then analysed in Matlab using Deproj to analyse cellular eccentricity (86).

Bayesian Force Inference of epithelium - Z projections and segmentation masks of R4/R5 tile scans were generated from Z-stacks as described above using localzprojector and cellpose respectively. Segmentation masks were then run through TissueAnalyser to produce coordinate data files of cell edges and vertices within the segmentation mask (87). Coordinate files were then processed in BayesianForceInference programme in MATLAB to generate tension and pressure data(19).

Stiffness (Nanoindentation) - Acquired force-displacement curves (*F-z*) were loaded in the graphical user interface (GUI) Nanoprepare (83), which was used to clean the data by deselecting any curves with failed contact or inappropriate noise. Collating

this cleaned data set, formal data analysis was carried out on the approach segment of the curve in the GUI SofTMech (83). The curves were then filtered to smooth any background noise generated by movement through the solution before contact. The segment denoting force applied (forward segment) to the midgut was then isolated. The contact point was defined by a threshold algorithm, transforming the curves from *F-z* to force-indentation ($F–\delta$). To these $F–\delta$ curves, the Hertz model was applied to the max indentation of $\delta = 0.1R$ to quantify the elastic property or stiffness (Pa) of the midguts.

GRASP signal – GRASP positive cells were detected by immunostaining for GFP. Zeiss 780 confocal microscope was used to manually count the number of GRASP+ cells per posterior midgut.

*lacZ* reporters – Antibodies against β-galactosidase were used to detect btl-lacZ reporters. Images were taken using confocal microscopy and staining was quantified using ImageJ. For each gut quantified, the background staining signal was subtracted from the total signal of β-galactosidase detected in the TTCs, ISCs/EBs or ECs. This value was then divided by the background signal to normalise the data.

Myc and Bnl staining – Midguts stained with antibodies to detect these proteins included a methanol fixation step between the paraformaldehyde fixation and PBST wash steps of the standard protocol, as described previously (36). Images were acquired using confocal microscopy and staining was quantified using ImageJ (Version 1.54f). For each quantified gut, the background staining signal was subtracted from the total antibody signal in DAPI+ cells. This value was then divided by the background signal to normalize the data.

Tracheal expression of *piezo* gene and Piezo protein trap - Quantifications were generated from a single z-stack of the R4 region for each midgut by confocal microscope and analysis was performed using ImageJ (Version 1.54f). A maximum intensity projection was produced for all images and channels were split. A skeleton was created in the channel corresponding to the gut trachea and threshold adjusted accordingly to ensure good selection of all tracheal branches. A region of interest was created from the trachea and applied to the *piezo* gene or Piezo protein trap expressing channel and fluorescence intensity quantified.

Tracheal GCamp signal - Quantifications were generated from a single z-stack of the R4 region for each midgut by confocal microscopy and analysis was performed using ImageJ (Version 1.54f). A maximum intensity projection was produced for all images and channels were split. A skeleton was created in the channel corresponding to the gut trachea (red) and threshold adjusted accordingly to ensure good selection of tracheal branches. A region of interest was created from the active GCamp expressing trachea (green) and applied to the general trachea expressing channel (red) and fluorescence intensity quantified.

Yki::GFP reporter – Quantifications were generated from a single Z stack of the R4 region of each midgut by confocal microscope and analysis was performed using ImageJ (Version 1.54f). A single Z plane was used to quantify each body cell where the nucleus was visible. Intensity of GFP was measured in the cytoplasm and the nucleus of each body cell and a ratio of nuclear to cytoplasmic intensity was generated to quantify nuclear translocation.

Mouse models

All mouse experiments were performed in accordance with the UK Home Office and ARRIVE guidelines and were reviewed by the Animal Welfare and Ethical Review Board of the University of Glasgow. Experiments were performed under PPL PP7226959 and PP6345023. Transgenic mouse strains were backcrossed with C57Bl6J for 10 generations prior to experimental work. *Pfgfb-CreER* were bred to *Piezo fl/fl* to generate cohort (*CreER;Piezo*$^{fl/fl}$) and control (*CreER;Piezo*$^{wt/wt}$) animals. Both male and female mice between 8-16 weeks of age were used for experiments. Mice were induced by 200µl of 15mg/ml Tamoxifen (Sigma T5648) in corn oil by oral gavage on two consecutive days. For regeneration experiments, mice were exposed to 10Gy whole body irradiation using the Xtrahl irradiator 5 days after Tamoxifen administration and then sampled 72 hours post radiation treatment. Non-irradiated, tamoxifen treated mice were harvested 8 days post induction for assessment of intestinal homeostasis. Equal numbers of males and females, which were matched in the control and cohort groups were used. Intestines were flushed with cold PBS and sections taken for wholemount immunostaining and cryosections which were snap frozen in OCT. Ten x 1cm sections from the duodenum and jejenum were

wrapped in surgical tape to make parcels and fixed in 4 percent paraformaldehyde overnight..

Immunohistochemistry of mouse tissue samples

All haematoxylin and eosin (H&E), immunohistochemistry (IHC), Alcian Blue (AB) and dual *in-situ* hybridization immunofluorescence (ISH-IF) staining was performed on 4µm formalin fixed paraffin embedded sections (FFPE) which had previously been ovened at 60□C for 2 hours. FFPE sections for c-Myc (ab32072, Abcam), chromogranin A (ab15160, Abcam) and Sox 9 (AB5535, Millipore) staining were stained using an Agilent autostainer Link48. H&E staining was performed on a Leica autostainer (ST5020). Staining for AB was performed manually on FFPE sections that were dewaxed and rehydrated through xylene and a graded ethanol series before washing in water. Rehydrated slides were stained for 10 minutes in Alcian Blue solution before rinsing in tap water and then counterstained with Eosin for 30 seconds.

RNAscope of mouse tissue samples

Dual *ISH-IF* detection for Pecam1 (316728-C2) and Piezo (500518-C1), 3-plex negative probe (320878) and 3-plex positive probe (320885) (all Bio-Techne) mRNA was performed using Multiplex fluorescent kit (322800; Bio-Techne) strictly according to the manufacturer's instructions. The staining was visualised staining with Opal dyes (FP1487001KT, FP1488001KT, Akoya Biosciences). To complete staining, sections were placed in a 60ºC oven for 30 minutes till dry, then sections were cover slipped using Ecomount (320409, Bio-Techne).

Whole mount Immunostaining of mouse small intestine

Samples were prepared using a protocol adapted from (64). Sections of small intestine were flushed with cold PBS, cut open and pinned longitudinally on silicone plates. Sections were then fixed overnight in 4 percent PFA at 4 degrees on a shaker. Samples were then washed in PBS before washing in 10 percent sucrose in PBS and then 20 percent sucrose with 10 percent glycerol in PBS. Samples were then dipped in 0.1 percent sodium azide for sample preservation. Some sections were stored in sodium azide for up to 3 months at 4 degrees for further immunostaining. Samples were then washed in PBS before being placed in blocking buffer (PBS 5

percent donkey serum, 0.5 percent BSA, 0.3 percent Triton, 0.1 percent sodium azide) for 2 hours before incubation with primary antibody for 48 hours at 4 degrees. Primary antibodies were diluted to the following concentrations in blocking buffer: chicken anti-GFP (1:400, Abcam), rat anti-Pecam (1:400, Cell Signalling), rabbit anti-Ecadherin (1:500, Cell Signalling). Samples were then washed in blocking buffer before incubation in secondary antibody for 16 hours at 4 degrees. All secondary antibodies were diluted in blocking buffer to a concentration of 1:500. Samples were washed in wash buffer (PBS 0.3 percent Triton) before post fixation in 1 percent PFA at 4 degrees overnight. Samples were washed in PBS before mounting. Small strips 1-2 villi thick were cut from intestine sections and mounted in Vectashield with DAPI. Images were acquired on a Zeiss 880. Vascular coverage was quantified using the Mexican Hat filter and Skeletonise plugins on Z projections of villi in ImageJ (Version 1.54f). Epithelial quantifications were performed the same way as in the *Drosophila* model using LocalZprojector, cellpose and Deproj. Five crypts per mouse were chosen at random.

**Statistics**

Data were analysed using two-way ANOVA with Sidak's multiple comparisons or T-test as indicated where P>0.05 was statistically significant. Results were analysed using Prism Graphpad. Individual sample data points are shown with group means presented as mean + standard error, where *P=0.05, ** P = 0.01, *** P=0.001 and **** P= 0.0001.

**Key Resources Table**

| **REAGENT OR RESOURCE** | **SOURCE** | **IDENTIFIER** |
|---|---|---|
| **Antibodies** | | |
| rat anti-Bnl | M. Krasnow | (88) |
| Chicken anti- βeta-Galactosidase, 1:400 | Abcam | ab-9361 |
| Rabbit anti-Chromogranin A, 1:700 | Abcam | ab15160 |
| Chicken anti-GFP, 1:4000 | Abcam | ab-13970 |
| Rabbit anti-DsRed | Clontech | 632496 |
| Guinea pig Anti-dMyc | Gift from G.Morata | N/A |

| | | |
|---|---|---|
| Rabbit Anti-c-Myc, 1:200 | Abcam | ab32072 |
| Mouse anti-Dlg 1:100 | DSHB | 528203 |
| Rabbit Anti-Ki67 | Cell Signalling Technology | 12202 |
| Rabbit Anti-Sox-9 | Millipore | AB5535 |
| Rabbit anti pH3 S10, 1:100 | Cell Signaling | NEB-9701 |
| Mouse anti pH3 S10, 1:100 | Cell Signaling | 9706S |
| Rabbit anti-p-Src 1:100 | Invitrogen | 44660G |
| Rat anti-Pecam1 1:500 | BD Pharmingen | 557355/MEC13.3 1 |
| Rabbit anti-Ecadherin 1:500 | Cell Signalling | 24E10 |
| RNAscope *Mm-Piezo1-O1* | ACDBio | 500518 |
| RNAscope *Mm-Pecam1-C2* | ACDBo | 316728-C2 |
| Goat Alexa Fluor anti-chicken IgY 488, 1:100 | Invitrogen | A11039 |
| Goat Alexa Fluor anti-chicken IgY 594, 1:100 | Invitrogen | A11042 |
| Goat Alexa Fluor anti-mouse IgG 488, 1:100 | Invitrogen | A11029 |
| Goat Alexa Fluor anti-mouse IgG 594, 1:100 | Invitrogen | A11032 |
| Goat Alexa Fluor anti-mouse IgG 647, 1:100 | Invitrogen | A21235 |
| Goat Alexa Fluor anti-Rabbit IgG 488, 1:100 | Invitrogen | A11008 |
| Goat Alexa Fluor anti-Rabbit IgG 594, 1:100 | Invitrogen | A11034 |
| Donkey Alexa Fluor anti-Rat IgG 594, 1:100 | Invitrogen | A21209 |
| Opal 520 | Akoya Biosciences | FP1487001KT |
| Opal 570 | Akoya Biosciences | FP1488001KT |
| **Chemicals** | | |
| NAC | Sigma | A7250 |
| Sucrose | Fisher | S/8600/60 |

| | | |
|---|---|---|
| | Chemical | |
| Yoda1 | Tocris | 5586 |
| Methylcellulose | Sigma | 274429 |
| DSS | Sigma | 42867-5G |
| Formaldehyde | FA, EM grade, | 30525-89-4 |
| Tamoxifen | Sigma | T5648 |
| Triton X100 | Sigma | X-100-1L |
| Normal Goat serum | Abcam | ab7481 |
| Vectashield with DAPI | Vector Laboratories | H-1200 |
| Bovine Serum Albumin | Sigma | A3294-50G |
| Schnieder's Medium | Sigma | 50146 |
| Fly Extract | VDRC | |
| Pen-Strep | Invitrogen | 15140 |
| Whatman GF/B Glass microfiber filters 21mm | Cytiva | 1821-021 |
| Corn Oil | Sigma | C8267 |
| QuikSil | World Precision Instruments | |
| DHE | Invitrogen | D23107 |
| DMSO | ThermoFisher | J66650.AK |
| Cell-Tak | Sigma | CLS354240 |
| Low gelling temperature agarose | Sigma | A4018 |
| FBS | Sigma | F4135 |
| Ecomount | Bio-Techne | 320409 |
| Sodium Azide | Sigma | 26628-22-8 |
| **Plasmids and primer sequences** | | |
| pJFRC19 | Addgene | Cat No 26224 |
| *lexAop-Src* (forward) *AGATCTGCGGCCGCATCCTCTAGAGTCGATCGACAT* | Thermo Fisher Scientific | N/A |
| *lexAop-Src* (reverse) *AGGTACCCTCGAGCCTGCAGGCATGCAAGCTT* | Thermo Fisher Scientific | N/A |

| **Experimental models: *Drosophila melanogaster* strains:** | | |
|---|---|---|
| *Wild type strain ($w^{1118}$)* | Gift from Ross Cagan | N/A |
| *dSRF-gal4, UAS-CD8GFP* | Gift from Irene Miguel-Aliaga | (89) |
| *esg-gal4, UAS-CD8GFP; tub-gal80$^{ts}$* | S. Hayashi | (90) |
| *esg-lexA* | Bloomington Drosophila Stock Center | 66632 |
| *lexAop-GFP* | Bloomington Drosophila Stock Center | 32210 |
| *esg-lexA, lexAop-GFP* | Generated in the Cordero lab | N/A |
| *piezo-gal4* | Gift from Norbert Perrimon | (35) |
| *QF6, QUAS mtdTomato* | Gift from Chrysoula Pitsouli | (15) |
| *Mex-gal4, tub-gal80$^{ts}$* | Gift from Irene Miguel-Aliaga | N/A |
| *UAS-piezo-IR1* | Bloomington Drosophila Stock Center | 2796 |
| *UAS-piezo-IR2* | Bloomington Drosophila Stock Center | 105132 |
| *btl-lacZ* | Bloomington Drosophila Stock Center | 12086 |
| *bnl-lacZ* | Bloomington Drosophila Stock Center | 11704 |
| *Yki::GFP* | Gift from Barry Thompson | (91) |
| *UAS-GC3Ai* | Gift from Andrew Davidson | N/A |
| *UAS-Yki-IR1* | Bloomington *Drosophila* Stock Center | 31965 |
| *UAS-Yki-IR2* | Bloomington *Drosophila* Stock Center | 34067 |
| *UAS-Yki$^{CA}$* | Bloomington *Drosophila* Stock Center | 28817 |
| *lexAop-Src* | Generated in the Cordero lab for this study | N/A |

| | | |
|---|---|---|
| *lgl::mcherry* | Gift from Eurico Morais-de-Sá | N/A |
| *btl-LexA* | Gift from Thomas Kornberg | (92) |
| *UAS-GFP1-10, lexAop-GFP11* | Gift from Thomas Kornberg | N/A |
| *lexAop-Cherry-CAAX* | Gift from Thomas Kornberg | (93) |
| *QUAS-GCamp6m* | Bloomington *Drosophila* Stock Center | 91988 |
| *Piezo::GFP mimic* | Bloomington *Drosophila* Stock Center | 60209 |
| *UAS-Piezo-EGFP* | Bloomington *Drosophila* Stock Center | 58772 |
| *UAS-bax, tubgal80$^{ts}$* | Gift from Cedric Polesello | N/A |
| **Mouse Strains** | | |
| *Pdgfb-CreER* | Marcus Fruttiger | (63) |
| *Piezo1$^{fl/fl}$* | Jackson Laboratories | 029213 |

**Detailed Genotypes:**

Figure 1

1. *dSRF-Gal4, UAS-CD8GFP/+; tub-Gal80$^{ts}$/+*
2. *dSRF-Gal4, UAS-CD8GFP/lgl::mcherry; MKRS/+*
3. *dSRF-Gal4, UAS-CD8GFP/+; tub-Gal80$^{ts}$/+*
4. *dSRF-Gal4, UAS-CD8GFP/lgl::mcherry; tub-Gal80$^{ts}$/+*
5. *Pdgf-beta Cre-GFP Piezo$^{wt/wt}$ (C57BL/6)*

Extended data Figure 1

1. *dSRF-Gal4, UAS-CD8GFP/+; tub-Gal80$^{ts}$/+*

Figure 2

1. *dSRF-Gal4, UAS-CD8GFP/lgl::mcherry; tub-Gal80$^{ts}$/+*
2. *dSRF-Gal4, UAS-CD8GFP/+; tub-Gal80$^{ts}$/+*
3. *Mex-Gal4/Btl-LexAHG, lexAop-Cherry-CAAX; UAS-GFP1-10, lexAop-GFP11/tub-Gal80$^{ts}$*
4. *Mex-Gal4/+; UAS-GFP1-10, lexAop-GFP11/tub-Gal80$^{ts}$*
5. *Btl-LexAHG, lexAop-Cherry-CAAX/+; UAS-GFP1-10, lexAop-GFP11/tub-Gal80$^{ts}$*

Figure 3

1. *Mex-Gal4/UAS-Bax, tub-Gal80$^{ts}$; QF6::QUAS-TdTomato/tub-Gal80$^{ts}$*
2. *Mex-Gal4/UAS-Bax, tub-Gal80ts; tub-Gal80$^{ts}$/MKRS*
3. *Mex-Gal4/lgl::mcherry; UAS-GC3Ai/MKRS*

4. *Mex-Gal4/+; tub-Gal80$^{ts}$/UAS-p35*
5. *Mex-Gal4,tub-Gal80$^{ts}$/+; QF6::QUAS-TdTomato/UAS-p35*
6. *Mex-Gal4/+; tub-Gal80$^{ts}$/UAS-p35*

Figure 4

1. *Piezo-Gal4/+; UAS-mCD8GFP/QF6::QUAS-TdTomato*
2. *dSRF-gal4, UAS-CD8GFP/+; tub-gal80$^{ts}$/+*
3. *dSRF-gal4, UAS-CD8GFP/UAS-piezo-IR2; tub-gal80$^{ts}$/+*
4. *dSRF-gal4, UAS-CD8GFP/+; tub-gal80$^{ts}$/UAS-piezo-IR1*
5. *dSRF-Gal4, UAS-CD8GFP/+; tub-Gal80$^{ts}$/+*
6. *dSRF-Gal4, UAS-CD8GFP/UAS-Piezo-EGFP; tub-Gal80$^{ts}$/+*
7. *Piezo-Gal4/+; UAS-mCD8GFP/QF6::QUAS-TdTomato*
8. *QF6::QUAS-TdTomato/QUAS-GCamp6m*

Extended data Figure 2

1. *Piezo::GFP mimic/ QF6::QUAS-TdTomato*
2. *Piezo-Gal4/+; UAS-mCD8GFP/QF6::QUAS-TdTomato*
3. *dSRF-Gal4, UAS-CD8GFP/+; tub-Gal80$^{ts}$/+*
4. *dSRF-Gal4, UAS-CD8GFP/+; tub-Gal80$^{ts}$/UAS-PiezoIR1*
5. *QF6::QUAS-TdTomato/QUAS-GCamp6m*

Figure 5

1. *dSRF-gal4, UAS-CD8GFP/+; tub-gal80$^{ts}$/+*
2. *dSRF-gal4, UAS-CD8GFP/UAS-piezo-IR2; tub-gal80$^{ts}$/bnl-lacZ*
3. *dSRF-gal4, UAS-CD8GFP/+; tub-gal80$^{ts}$/+*
4. *dSRF-gal4, UAS-CD8GFP/+; tub-gal80$^{ts}$/UAS-piezo-IR1*
5. *Yki::GFP/ Yki::GFP; QF6, QUAS mtdTomato/+*

Figure 6

1. *dSRF-gal4, UAS-CD8GFP/+; tub-gal80$^{ts}$/+*
2. *dSRF-gal4, UAS-CD8GFP/+; tub-gal80$^{ts}$/UAS-Yki-IR1*
3. *dSRF-gal4, UAS-CD8GFP/UAS-Yki-IR2; tub-gal80$^{ts}$/+*
4. *dSRF-gal4, UAS-CD8GFP/+; tub-gal80$^{ts}$/ UAS-Yki$^{CA}$*

Extended data Figure 3

1. *dSRF-gal4, UAS-CD8GFP/+; tub-gal80$^{ts}$/btl-lacZ*
2. *dSRF-gal4, UAS-CD8GFP/UAS-piezo-IR2; tub-gal80$^{ts}$/btl-lacZ*

Figure 7

1. *Pdgf-beta CreER-GFP Piezo$^{wt/wt}$ (C57BL/6)*
2. *Pdgf-beta CreER-GFP Piezo$^{fl/fl}$ (C57BL/6)*
3. *esg-lexA, LexAop-GFP/+; QF6::QUAS-TdTomato/ tub-Gal80$^{ts}$*
4. *esg-lexA, lexAop-GFP/lexAopSrc; QF6::QUAS-TdTomato/ tub-Gal80$^{ts}$*
5. *esg-lexA/Piezo::GFP mimic; QF6::QUAS-TdTomato/ tub-Gal80$^{ts}$*
6. *esg-lexA/dSRF-Gal4, UAS-CD8GFP; UAS-PiezoIR1/ tub-Gal80$^{ts}$*
7. *esg-lexA/dSRF-Gal4, UAS-CD8GFP; +/lexAop-Src, tub-Gal80$^{ts}$*

8. *esg-lexA/dSRF-Gal4, UAS-CD8GFP; +/tub-Gal80$^{ts}$*
9. *esg-lexA/dSRF-Gal4, UAS-CD8GFP; UAS-PiezoIR1/lexAop-Src, tub-Gal80$^{ts}$*

Extended data Figure 4

1. *Pdgf-beta CreER-GFP Piezo$^{wt/wt}$ (C57BL/6)*
2. *Pdgf-beta CreER-GFP Piezo$^{fl/fl}$ (C57BL/6)*
3. *esg-lexA, lexAop-GFP/+; QF6::QUAS-TdTomato/ tub-Gal80$^{ts}$*
4. *esg-lexA, lexAop-GFP/lexAop-Src; QF6::QUAS-TdTomato/ tub-Gal80$^{ts}$*

## Figure Legends

**Fig 1. Morphological changes in the regenerating adult intestine occur in parallel of tracheal/vascular remodelling. a, b.** Representative confocal images of the adult *Drosophila* midgut associated trachea (green) in the context of sucrose and *Pe* (**a**) or DSS (**b**) feeding. Scale bars, 20 microns. **a', b'**. Quantification of tracheal remodelling as in a (n=21,21) and b (n=21,23), respectively. **c.** Overview of adult *Drosophila* midgut in the context of sucrose and *Pe* feeding. Posterior midgut regions are shaded in red. Anterior-posterior (A.P.) and dorsal-central (D.V) lengths are marked with arrows. Scale bar, 100 microns. **d, e.** Quantification of anterior-posterior (A/P) (**d**) and dorsal-ventral (D/V) (**e**) lengths from midguts as in c (n=22,21,22,21). **f.** Overview of adult *Drosophila* midgut in the context of sucrose and DSS feeding. Posterior midgut regions are shaded in red. Anterior-posterior (A.P.) and dorsal-central (D.V) lengths are marked with arrows. Scale bar, 100 microns. **g, h.** Quantification of gut A/P (**g**) and D/V (**h**) length from midguts as in f (n=12,21,12,17). **i**. Confocal images of the intestinal epithelium in the context of sucrose feeding and *Pe* infection. *lgl*::mcherry labels cell junctions (red) and DAPI labels all cell nuclei (white). Scale bar, 20 microns. **i'**. Representative images of epithelial eccentricity in midguts as in i. More eccentric cells have a value close to 1 indicated by the yellow colouring and more circular cells have a value close to 0 indicated by the blue colouring. Scale bar, 10 microns. **j**. Quantification of epithelial eccentricity as in i'. Smaller circles in the background indicate individual cell values and large outlined circles indicate the average cell eccentricity value per gut analysed. Each colour indicates a different biological replicate. (n=13, 12). **k**. Confocal images of the intestinal epithelium in the context of sucrose feeding and DSS damage. *lgl*::mcherry labels cell junctions (red) and DAPI labels all cell nuclei (white). Scale bar, 20 microns. **k'**. Representative images of cellular eccentricity in

midguts as in k. Scale bar, 10 microns. **l**. Quantification of epithelial eccentricity as in k'. Smaller circles in the background indicate individual cell values and large outlined circles indicate the average cell eccentricity value per gut analysed. Each colour indicates a different biological replicate (n=5,5). **m**. Confocal images of posterior midgut of flies fed normal food (NF) or methylcellulose (MC). Posterior midgut region is shaded in red, and A/P and D/V lengths are marked with arrows. Scale bar, 100 microns. **n, o.** Quantification of A/P length (**n**) and D/V axis (**o**) from midguts as in m (n=12,22,12,22) **p**. Confocal images of epithelial cells in the midgut of flies fed normal food (NF) or methylcellulose (MC). *lgl*::mcherry labels cell junctions (red) and DAPI labels all cell nuclei (white). Scale bar, 20 microns. **p'**. representative images of eccentricity in midguts as in p. **q**. Quantification of eccentricity as in p'. Smaller circles in the background indicate individual cell values and large outlined circles indicate the average cell eccentricity value per gut analysed. Each colour indicates a different biological replicate (n=11,13) **r**. Representative confocal images of midgut associated trachea (green) in the context of normal food (NF) or methylcellulose (MC) feeding. Scale bar, 20 microns. **s**. Quantification of tracheal coverage in midguts as in r (n=19,34). **t.** Confocal images of mouse intestinal crypts from control (non-irradiated) and irradiated mice 72 hours post treatment. Images are produced using wholemount immunostaining and cell boundaries are detected using E-cadherin staining (red); DAPI (blue). Scale bar, 20 microns. **t'**. Representative image of epithelial eccentricity in mouse crypts as in t. **u**. Quantification of epithelial eccentricity as in t'. Smaller circles in the background indicate individual cell values and large outlined circles indicate the average cell eccentricity value per gut analysed (n=6,5). **v**. Wholemount immunostaining of crypt vasculature using Pecam-1 (green) in the context of homeostasis (non-irradiated) and 72 hours post whole-body irradiation (irradiated). Cell boundaries are detected using E-cadherin staining (red). Scale bar, 20 microns. **w**. Quantification of crypt vascular branches in intestines as in v (n=3,6). Data represent the mean ± s.e.m. n numbers indicated for each graph are listed from left to right and correspond to the numbers of guts analysed. Statistics: Two-tailed unpaired Student's t-test. *P=0.05, ** P = 0.01, *** P=0.001 and **** P= 0.0001. DAPI, 4,6-diamidino-2-phenylindole.

**Fig 2**. **Enterocytes experience significant mechanical changes upon damage. a.** Overview of an adult *Drosophila* gut with R1-R5 regions labelled. Scale bar, 100 microns. **b, c** Confocal images of trachea (**b**) and intestinal epithelium (**c**) from R4 and R5 regions of the posterior midgut in the context of Sucrose or *Pe* infection. Scale bar, 20 microns. **d**. Quantification of tracheal coverage in the R4 and R5 regions of the midgut upon *Pe* infection. (n=6,6,6,6). **e**. Quantification of cell aspect ratio in R4 and R5 regions of the gut upon infection. Each data point represents an individual enterocyte. (n =6,6,6,6). **f**. Tilescans across the R4 and R5 regions of the posterior midgut where enterocytes cell junctions have been detected with lgl (green). Scale bar, 50 microns. **f'**. Representative image of inferred relative cell pressure calculated using Bayesian Force Inference. Cells of higher pressure are red/yellow and lower pressure cells blue/green. **g**. Quantification of relative pressure across the R4 (grey) and R5 (green) regions of the midgut upon sucrose feeding or *Pe* infection, measured by Bayesian Force Inference in MATLAB. Smaller circles represent individual cells and larger circles in foreground represent average of cells per gut (n=4,4,5,5). **h**. Representative image of nanoindentation setup. *Drosophila* gut is placed on cell-Tak adhesive and cantilever is used to detect stiffness by touching the outside of the gut. **i**. Quantification of stiffness across midgut R4 and R5 regions using nanoindentation in the context of sucrose feeding or *Pe* infection. Smaller circles represent individual measurements within a gut (n=4,5,5,3). **j**. Overview of GFP reconstitution across synaptic partners (GRASP) system. Components of a split GFP barrel are expressed in two different cell types where close contact results in GFP reconstitution and fluorescence. When expressed in the trachea (*btl-lexA*; red) and enterocytes (*Mex-gal4)* GFP (green) reconstitution is observed upon *Pe* damage as a result of close contact. **k**. Confocal images of GRASP expression in the intestinal epithelium and surrounding trachea following sucrose or *Pe* infection. Scale bar, 20 microns. **l**. Quantification of the number of GRASP positive cells per posterior midgut (n=20,23). **m, n**. Controls without *btl-lexA* driver system (**m**) and without *Mex-Gal4* driver system (**n**). Scale bar, 20 microns. Data represent the mean ± s.e.m. n numbers indicated for each graph are listed from left to right and they correspond to the numbers of guts analysed. Statistics: **l**. Two-tailed unpaired Student's t-test. **d, e, g, i.** Two-way ANOVA followed by Tukey's multiple comparisons test *P=0.05, ** P = 0.01, *** P=0.001 and **** P= 0.0001. DAPI, 4,6-diamidino-2-phenylindole.

**Fig 3. Cell death is necessary and sufficient for mechanical changes and tracheal remodelling in the regenerating intestine. a.** Representative confocal images of midgut associated trachea (*QF>mtdTomato*; red) in wildtype midgut or following *bax* overexpression in enterocytes (*Mex$^{ts}$>bax*). Scale bar, 20 microns. **b**. Quantification of tracheal coverage in midguts as in a (n=6,11). **c**. Confocal images of enterocytes detected by Dlg staining (red) in wildtype midgut or following *bax* overexpression in enterocytes (*Mex$^{ts}$>bax*). Scale bar, 20 microns. **c'**. Representative image of eccentricity quantification in midguts as in c. More eccentric cells have a value closer to 1 in yellow and more circular cells have a value close to 0 in blue and green. **d**. Eccentricity quantification as in c'. Smaller circles in the background indicate individual cell values and large outlined circles indicate the average cell eccentricity value per gut analysed. Each colour indicates a different biological replicate (n=11,14). **e**. Confocal images of midgut expressing an apoptotic sensor (GC3Ai; green) in enterocytes (*Mex-Gal4*) and cell boundary marker (*lgl::mCherry*; red) at 2 hours post infection. The righ panel shows a zoom of area indicated by the dotted box in left panel. Arrow points to an individual apoptotic cell. Scale bar, 20 microns. **e'.** Segmentation of cell boundaries in midgut as in e. Apoptotic cell (orange; arrow) and Row1 (red) and Row3 (blue) from apoptotic cell are highlighted. **e''**. Representative image of epithelial eccentricity as in e. Row1 and Row3 are labelled as in e'. Arrow points to an individual apoptotic cell. **f**. Quantification of epithelial eccentricity in cells witin Row1 and Row3 from apoptotic cell after 2 hours of *Pe* infection (n=3,3). **g**. Confocal images of the epithelium (Dlg; red) in wildtype midguts or following *p35* overexpression in enterocytes (*Mex$^{ts}$>p35*) upon sucrose or *Pe* feeding. Scale bar, 20 microns. **g'** Representative images of eccentricity in midguts as in g. **h**. Quantification of eccentricity as in g' (n=9,8,9,8). **i**. Quantification of stiffness (young's modulus) in measured using nanoindentation in midguts as in g. Smaller dots in the background represent individual cells and larger circles in the foreground represent average per gut (n=3,3,3,3). **j**. Confocal images of the trachea (*QF>mtdTomato*; red) in wildtype midguts or following *p35* overexpression in enterocytes (*Mex$^{ts}$>p35*) upon sucrose or *Pe* feeding. Scale bar, 20 microns. **K**. Quantification of tracheal remodelling from midguts as in j (n=9,12,3,7). **l**. Confocal images of DHE staining (red) in midguts as in j. Scale bar,

20 microns. **m**. Quantification of DHE staining from midguts as in l (n=11,10,11,13). Data represent the mean ± s.e.m. n numbers indicated for each graph are listed from left to right and they correspond to the numbers of guts analysed. Statistics: **b, d, f.** Two-tailed unpaired Student's t-test. **h, j, k, m.** Two-way ANOVA followed by Tukey's multiple comparisons test ** P = 0.01, *** P=0.001 and **** P= 0.0001. DAPI; 4,6-diamidino-2-phenylindole. DHE; Dihydroethidium.

**Fig 4. Piezo activity dictates tracheal remodelling and ISC proliferation in the *Drosophila* intestine. a.** Confocal images of midgut associated trachea (*QF>mtdTomato*; green pseudocoloured) and *piezo* expression (magenta) in flies treated with Sucrose, Pe or DSS. Arrows point to a *piezo* negative tracheal cell. Scale bar, 20 microns. **b**. Quantification of *piezo* expression relative to total tracheal coverage in midguts as in a (n=24,9,22). **c**. Confocal images of midgut associated trachea (*QF>mtdTomato*; green pseudocoloured) and *piezo* expression (magenta) following Yoda1 treatment. Scale bar, 20 microns. **d**. Quantification of *piezo* expression relative to total tracheal coverage in midguts as in c (n=22,24). **e, f.** Quantification of tracheal coverage (**e**) (n=23,30) and ISC proliferation (PH3+) (**f**) (n=23,30) in midguts as in c. **g**. Representative confocal images of the midgut associated trachea (*dSRF$^{ts}$>gfp*; green) in the context sucrose feeding, *Pe* infection or DSS feeding in control animals or following RNAi *piezo* knockdown in trachea (*piezo-IR1)*. Scale bar, 20 microns. **h, i.** Quantification of tracheal coverage (**h**) (n=23,19,8,21,23,14,13,14) and ISC proliferation (PH3+) (**i**) (n=14,19,9,30,23,11,13,14) in midguts as in g. **j**. Representative confocal images of midgut associated tracheal tissue (*dSRF$^{ts}$>gfp*; green) in control or tracheal *piezo* overexpressing animals upon 0 and 16hs of *Pe* infection or 48hs after *Pe* removal (recovery). Scale bar, 20 microns. **k, l**. Quantification of tracheal coverage (**k**) (n=29,16,36,23,23,19) and ISC proliferation (**l**) (n=25,22,20,23,22,17) in midguts as in j. **m**. Confocal images of midgut associated trachea (*QF>mtdTomato*; green pseudocoloured) and *piezo* expression (magenta) across a time course of 0-16 hours of *Pe* infection**.** Scale bar, 20 microns. **n**. Quantification of tracheal *piezo* expression relative to total tracheal coverage in midguts as in m (n=14,19,11,25). **o**. Correlation graph between tracheal coverage and *piezo* expression in each of the time points represented in m. Pearson's correlation coefficient (r=0.9915). **p**.

Quantification of stiffness measured by nanoindentation (young's modulus) in midguts from timepoints as in m. Each dot represents a single measurement within a gut (n=3,3,3,3). **q**. Representative confocal images of trachea (*QF>mtdTomato*; red) and GCamp6m calcium sensor (green) of a *Pe* infection time course from 0 to 16 hours of *Pe* feeding. Scale bar, 20 microns. **r**. Correlation graph between tracheal coverage and GCamp6m signal in each of the time points represented in q. Pearson's correlation coefficient (r=0.7345). **s**. Close up still frames of GCamp6m *in vivo* live imaging in the context of *Pe* infection. Arrows indicate branches which show a calcium impulse prior to a remodelling event. Scale bar, 20 microns. Data represent the mean ± s.e.m. n numbers indicated for each graph are listed from left to right and they correspond to the numbers of guts analysed. Statistics: **b, d, e, f**.Two-tailed unpaired Student's t-test. **h, i, k, l, n, p.** Two-way ANOVA followed by Tukey's multiple comparisons test ** P = 0.01, *** P=0.001 and **** P= 0.0001. DAPI, 4,6-diamidino-2-phenylindole.

**Fig 5. Tracheal Piezo regulates Yki activity and remodelling pathways in gut associated trachea. a.** Representative confocal images of midgut associated trachea (*dSRF$^{ts}$>gfp*; green) and *bnl-LacZ* expression (grey) upon sucrose or *Pe* feeding in control midguts or following tracheal *piezo* knockdown (*piezo-IR1*). Scale bar, 20 microns. **b**. Quantification of *bnl-LacZ* expression per TTC in midguts as in a (n=18,16,22,22). **c**. Representative confocal images of midgut associated trachea (*dSRF$^{ts}$>gfp*; green) and Myc expression (magenta) upon sucrose or *Pe* feeding in control midguts or following tracheal *piezo* knockdown (*piezo-IR1*). Scale bar, 20 microns. **d**. Quantification of Myc intensity in TTCs as in c (n=18,23,13,26). **e**. Representative confocal images of midgut associated tracheal tissue (*QF>mtdTomato*; green pseudocoloured) and Yki::GFP (grey) in midguts from sucrore, *Pe* or DSS fed control or *Pe* fed animals following tracheal *piezo* knockdown (*piezo-IR1*). Scale bar, 20 microns. **f, g**. Quantification of Yki nuclear to cytoplasmic ratio in midguts as in e. Each data point represents a single tracheal body cell; **f** (n=10,10); **g** (n=8,7,8,10). Data represent the mean ± s.e.m. n numbers indicated for each graph are listed from left to right and they correspond to the numbers of guts analysed. Statistics: **f.** Two-tailed unpaired Student's t-test. **b, d, g.**Two-way

ANOVA followed by Tukey's multiple comparisons test *** P=0.001 and **** P= 0.0001. DAPI, 4,6-diamidino-2-phenylindole.

**Fig 6. Yki translates mechanical signals into tracheal remodelling in the *Drosophila* midgut. a.** Confocal images of trachea (*dSRF$^{ts}$>gfp*; green) upon sucrose or *Pe* feeding in control midguts or following tracheal *yki* knockdown (*yki-IR1*). Scale bar, 20 microns. **b, c.** Quantification of tracheal coverage (**b**) (n=9,9,9,11,11,11) and ISC proliferation (PH3+) (**c**) (n=10,9,10,11,12,12) in midguts as in a. **d**. Representative confocal images of midgut associated trachea (*dSRF$^{ts}$>gfp*; green) without (control) or with overexpression of constitutively active *Yki* (*Yki-CA*) upon 16hs of *Pe* infection or 48hs after *Pe* removal (recovery). Scale bar, 20 microns. **e, f.** Quantification of tracheal coverage (**e**) (n=16,17,20,14) and ISC proliferation (PH3+) (**f**) (n=16,17,20,14) in midguts as in d. **g**. Representation confocal images of midgut associated trachea (*dSRF$^{ts}$>gfp*; green) and anti-Bnl expression (grey) upon sucrose or *Pe* feeding in control midguts or following tracheal *yki* knockdown (*yki-IR1*). Scale bar, 20 microns. **h**. Quantification of Bnl expression per TTC in midguts as in g (n=15,18,18,16). **i**. Representative confocal images of midgut associated trachea (*dSRF$^{ts}$>gfp*; green) and Myc expression (magenta) upon sucrose or *Pe* feeding in control midguts or following tracheal *yki* knockdown (*yki-IR1*). Scale bar, 20 microns. **j**. Quantification of Myc expression per TTC in midguts as in i (n=14,16,13,18). Data represent the mean ± s.e.m. n numbers indicated for each graph are listed from left to right and they correspond to the numbers of guts analysed. **k**. Proposed working model of gut/tracheal mechanosensory crosstalk during intestinal regeneration in *Drosophila*. Statistics: Two-way ANOVA followed by Tukey's multiple comparisons test *P=0.05, ** P = 0.01, *** P=0.001 and **** P= 0.0001. DAPI, 4,6-diamidino-2-phenylindole.

**Fig 7. The role of vascular Piezo is conserved in mammalian intestinal regeneration and *Drosophila* intestinal hyperplasia. a.** Confocal images of single molecule RNA in situ detection of *Pecam-1* (red) and *Piezo-1* (green; grey) in mouse small intestinal crypts. DAPI (blue). Centre and right panels are magnified views of the area highlighted by the dotted box in the left panel. Arrows point to *Piezo-1* signal

within a crypt. Scale bar, 60 microns. **b**. Confocal images of wholemount preparation of intestinal tissue from *Pdgf-beta-CreER-GFP* mice. Cre expression (green); anti-Pecam-1 (grey). Scale bar, 20 microns. **c**. H and E and Ki67 staining of small intestinal samples from non-irradiated *Pdgf-beta-CreER Piezo1*$^{wt/wt}$ and *Piezo1*$^{fl/fl}$ mice. Scale bar, 20 microns. **d, e.** Quantification of the number of crypts per circumference (**d**) (n=6,6) and number of Ki67+ cells per intestinal crypt (**e**) (n=3,3) in mice as in c. **f**. Wholemount immunostaining of the crypt intestinal vasculature of irradiated *Pdgf-beta-CreER Piezo1*$^{wt/wt}$ and *Piezo1*$^{fl/fl}$ mice using anti-Pecam-1 antibody (green). Cell boundaries are detected using E-cadherin staining (red); DAPI (blue). Scale bar, 20 microns. **g**. Quantification of crypt vascular branch number in intestines as in f (n=6,6). **h**. H and E and Ki67 staining of small intestinal samples from irradiated *Pdgf-beta-CreER Piezo1*$^{wt/wt}$ and *Piezo1*$^{fl/fl}$ mice. Scale bar, 20 microns. **i, j**. Quantification of number of crypts per circumference (**i**) (n=6,6) and number of Ki67+ cells per intestinal crypt (**j**) (n=3,3) in mice as in h. **k.** Immunostaining of Myc and Sox9 in intestinal crypts of *Pdgf-beta-CreER Piezo1*$^{wt/wt}$ and *Piezo1*$^{fl/fl}$ mice following irradiation. Scale bars, 20 microns. **l, m.** Quantification of Myc (**l**) (n=6,6) and Sox9 (**m**) (n=6,6) as a percentage of staining positive cells per crypt in intestines as in k. **n**. Representative confocal images of adult *Drosophila* midgut from control flies or upon overexpression of *Src* in stem/progenitor cells (*esg-lexA*$^{ts}$). Posterior midgut regions are shaded in red. Anterior-posterior (A.P.) and dorsal-central (D.V) lengths are marked with arrows. Scale bar, 100 microns. **o, p.** Quantification of A/P length (**o**) (n=14,16) and D/V axis (**p**) (n=14,16) in midguts as in n. **q**. Confocal images of the intestinal epithelium of control flies or upon overexpression of *Src* in stem/progenitor cells (*esg-lexA*$^{ts}$). Enterocyte junctions are labelled with Dlg (grey) and progenitor cells express GFP (green). Scale bar, 20 microns. **q'**. Eccentricity representative images of epithelia from midguts as in q. **r**. Quantification of epithelial eccentricity as in q' (n=13,16). **s**. Confocal images of control flies or upon overexpression of *Src* in stem/progenitor cells (*esg-lexA*$^{ts}$) and stained with anti-phosphorylated Src (pSrc; green); Piezo expression (magenta); gut associated trachea (*Q6>mtdTomato*; red). Scale bar, 20 microns. **t**. Quantification of tracheal Piezo expression in midguts as in s (n=17,13). **u**. Confocal images of gut associated trachea (*dSRF*$^{ts}$*>gfp*; green) from control flies or upon overexpression of *Src* in stem/progenitor cells (*esg-lexA*$^{ts}$); with and without piezo knockdown (*piezo-IR1*) in tracheal cells. Scale bar, 20 microns. **v, w.** Quantification of ISC proliferation

(PH3+) (**v**) (n=26,20,22,19) and tracheal coverage (**w**) (n=22,26,25,29) in midguts as in u. Data represent the mean±s.e.m. n numbers indicated for each graph are listed from left to right and they correspond to the numbers of guts analysed. Statistics: **d, e, g, i, j, l, m, o, p, r, t**. Two-tailed unpaired Student's t-test. **v, w.** Two-way ANOVA followed by Tukey's multiple comparisons test *P=0.05, ** P = 0.01, *** P=0.001 and **** P= 0.0001. DAPI, 4,6-diamidino-2-phenylindole.

**Extended Data Fig 1. Mechanical changes in the intestine are sufficient to drive tracheal remodelling. a**. Representative confocal images of intestinal DHE staining (red) for reactive oxigene species detection in sucrose and *Pe* fed flies. Scale bar, 20 microns. **b**. Quantification of DHE intensity in midguts as in a (n=5,9). **c**. Confocal images of intestinal DHE staining (red) in sucrose and DSS fed flies. Scale bars, 20 microns. **d**. Quantification of gut DHE intensity in midguts as in c (n=13,14). **e**. Confocal images of midgut associated trachea (*dSRF$^{ts}$>gfp*; green) from sucrose and DSS fed flies with and without treatment with the anti-oxidant NAC. Scale bar, 20 microns. **f, g.** Quantification of tracheal coverage (**f**) (n=17,17,16,17) and ISC proliferation (PH3+) (**g**) (n=17,17,16,17) in midguts as in e. Data represent the mean±s.e.m. n numbers indicated for each graph are listed from left to right and they correspond to the numbers of guts analysed. Statistics: **b, d**. Two-tailed unpaired Student's t-test. **f, g.** Two-way ANOVA followed by Tukey's multiple comparisons test ** P = 0.01 and **** P= 0.0001. DHE; Dihydroethidium. NAC; N-acetylcysteine.

**Extended Data Fig 2. Mechanical changes in the intestine are sensed by tracheal Piezo. a.** Representative confocal images of trachea (*QF>mtdTomato*; green pseudocoloured) and Piezo (magenta) in in sucrose and *Pe* fed flies. Scale bar, 20 microns. **b**. Quantification of tracheal Piezo expression relative to tracheal coverage in midguts as in a (n=27,29). **c**. Quantification of tracheal coverage in midguts from sucrose and *Pe* fed flies with and without treatment with the anti-oxidant NAC (n=12,23,9,21). **d.** Representative confocal images of *piezo* expression (magenta) in midguts from sucrose and *Pe* fed flies with and without treatment with the anti-oxidant NAC. Scale bar, 20 microns. **e.** Quantification of *piezo* expression relative to tracheal coverage in midguts as in d (n=12,23,9,21). **f**. Confocal images of

trachea (*QF>mtdTomato*; green pseudocoloured) and *piezo* expression (magenta) in the posterior midgut after feeding with normal food (NF) or methylcellulose (MC). Scale bar, 20 microns. **g**. Quantification of tracheal *piezo* expression relative to tracheal coverage in midguts as in f (n= 6, 8). **h**. Confocal images of midgut associated trachea (*dSRF$^{ts}$>gfp*; green) following sucrose or Yoda1 feeding. Scale bar, 20 microns. **i**. Confocal images of the intestinal epithelium (anti-Dlg; red) of control flies or flies overexpressing Piezo RNAi (*piezo-IR1*) in tracheal cells, upon sucrose or *Pe* feeding. DAPI (blue). Scale bar, 20 microns. **i'**. Representative images of eccentricity in midguts as in i. **j**. Quantification of eccentricity in midguts as in i' (n=7,8,9,7). **k**. Still frames of *in vivo* live imaging of trachea (*QF>mtdTomato*; red) and GCamp6s calcium reporter (green) in sucrose or *Pe* fed control animals or upon tracheal knockdown of *piezo* (*piezo-IR1*) and Pe feeding. Scale bar, 20 microns. Data represent the mean±s.e.m. n numbers indicated for each graph are listed from left to right and they correspond to the numbers of guts analysed. Statistics: **b,g.** Two-tailed unpaired Student's t-test. **c, e, j.** Two-way ANOVA followed by Tukey's multiple comparisons test *P=0.05, ** P = 0.01, *** P=0.001 and **** P= 0.0001. DAPI, 4,6-diamidino-2-phenylindole. NAC; N-acetylcysteine.

**Extended Data Fig 3. Tracheal Btl is not regulated by Piezo. a.** Representative confocal images of gut trachea (*dSRF$^{ts}$>gfp*; green) and *btl-lacZ* (grey) upon sucrose or *Pe* feeding in control midguts or following tracheal *piezo* knockdown (*piezo-IR1*). Scale bar, 20 microns. **b**. Quantification of average *btl-lacZ* expression per TTC in midguts as in a (n=15,10,14,18). Boxed areas indicate regions selected for magnified view, which are presented in insets witin the grey scale panels. Data represent the mean±s.e.m. n numbers indicated for each graph are listed from left to right and they correspond to the numbers of guts analysed. Statistics: Two-tailed unpaired Student's t-test. *** P=0.001 and **** P= 0.0001. DAPI, 4,6-diamidino-2-phenylindole.

**Extended Data Fig 4. The role of vascular Piezo is conserved in mammalian intestinal regeneration and *Drosophila* intestinal hyperplasia. a.** Experimental design of mouse experiments. Mice were induced with 3mg Tamoxifen on two consecutive days by oral gavage and sacrificed at day 8 after induction. For the damage-induced regeneration model, mice were given 10 Gy whole body irradiation at day 5 after transgene induction and intestinal tissue sampled 72 hours later. **b**. Method used to segment and quantify vascular branching in whole mount

immunostaining of the intestinal vasculature using anti-Pecam-1 antibody. Confocal images are projected and a Mexican hat filter is applied before skeletonization. Scale bar, 20 microns. **c**. Whole mount immunostaining of anti-Pecam-1 (green) in crypt villus images of *Pdgf-beta-CreER Piezo1*$^{wt/wt}$ and *Piezo1*$^{fl/fl}$ mice without or with irradiation. **d**. Quantification of the number of vascular branches in non-irradiated (n=6,5) and irradiated (n=6,6) mice. **e**. Immunostaining of Chromogranin A for enteroendocrine cell detection in small intestinal samples from mice as in c. Scale bar, 20 microns. **f**. Quantification of Chromogranin A cells per crypt villus axis in non-irradiated (n=3,3) and irradiated (n=3,3) mice. **g**. Staining with Alcian blue for goblet cell detection in intestinal samples from animals as in c. Scale bar, 20 microns. **h**. Quantification of Alcian Blue cells per crypt villus axis in non-irradiated (n=3,3) and irradiated mice (n=3,3). **i**. Confocal images of control or *Src* overexpressing midgut stem progenitor cells (*esg-lexA*$^{ts}$; green) and surrounding tracheal tissue (*QF>mtdTomato*; red). DAPi (blue). Scale bar, 20 microns. **j, k.** Quantification of ISC proliferation (**j**) (n=14,13) and tracheal coverage (**K**) (n=19,23) in midguts as in i. Data represent the mean ± s.e.m. n numbers indicated for each graph are listed from left to right and they correspond to the numbers of guts analysed. Statistics: Two-tailed unpaired Student's t-test. **** P= 0.0001. DAPI, 4,6-diamidino-2-phenylindole.

**Supplementary Movie 1**

Time-lapse *in vivo* live imaging of a control *Drosophila* posterior midgut from Sucrose fed mated female fly. The general tracheal network was labelled with *Q6>mtdTomato* (red) and the calcium reporter *GCamp6s* (green) is expressed under the control of the tracheal driver *dSRF-gal4*. Fly was starved and then fed sucrose for 2 hours prior to imaging for 3 hours.

**Supplementary Movie 2**

Time-lapse *in vivo* live imaging of a control *Drosophila* posterior midgut from *Pe* fed mated female fly. The general tracheal network was labelled with *Q6>mtdTomato* (red) and the calcium reporter *GCamp6s* (green) is expressed under the control of the tracheal driver *dSRF-gal4*. Fly was starved and then fed *Pe* for 2 hours prior to imaging for 3 hours.

**Supplementary Movie 3**

Time-lapse *in vivo* live imaging of a *Drosophila* posterior midgut from *Pe* fed mated female fly. The general tracheal network was labelled with *Q6>mtdTomato* (red) and the calcium reporter *GCamp6s* (green) and a *piezo-RNAi* (*piezo-IR1*) are expressed under the control of the tracheal driver *dSRF-gal4*. Fly was starved and then fed *Pe* for 2 hours prior to imaging for 3 hours.

**References**


1. Hageman JH, Heinz MC, Kretzschmar K, Van Der Vaart J, Clevers H, Snippert HJG. Intestinal Regeneration: Regulation by the Microenvironment. Developmental Cell. 2020;54(4):435-46.
2. Sato T, Van Es JH, Snippert HJ, Stange DE, Vries RG, Van Den Born M, et al. Paneth cells constitute the niche for Lgr5 stem cells in intestinal crypts. Nature. 2011;469(7330):415-8.
3. Li H, Jasper H. Gastrointestinal stem cells in health and disease: from flies to humans. Disease Models & Mechanisms. 2016;9(5):487-99.
4. Barker N, Van Es JH, Kuipers J, Kujala P, Van Den Born M, Cozijnsen M, et al. Identification of stem cells in small intestine and colon by marker gene Lgr5. Nature. 2007;449(7165):1003-7.
5. Micchelli CA, Perrimon N. Evidence that stem cells reside in the adult Drosophila midgut epithelium. Nature. 2006;439(7075):475-9.
6. Ohlstein B, Spradling A. The adult Drosophila posterior midgut is maintained by pluripotent stem cells. Nature. 2006;439(7075):470-4.
7. Medina AB, Perochon J, Johnson C, Polcowñuk S, Tian Y, Yu Y, et al. Neuroendocrine Control of Intestinal Regeneration Through the Vascular Niche in*Drosophila*. 2024.
8. Touhara KK, Rossen ND, Deng F, Castro J, Harrington AM, Chu T, et al. Topological segregation of stress sensors along the gut crypt–villus axis. Nature. 2025.
9. Miguel-Aliaga I, Jasper H, Lemaitre B. Anatomy and Physiology of the Digestive Tract of *Drosophila melanogaster*. Genetics. 2018;210(2):357-96.
10. Vereecke L, Beyaert R, van Loo G. Enterocyte death and intestinal barrier maintenance in homeostasis and disease. Trends in Molecular Medicine. 2011;17(10):584-93.
11. Ding B-S, Cao Z, Lis R, Nolan DJ, Guo P, Simons M, et al. Divergent angiocrine signals from vascular niche balance liver regeneration and fibrosis. Nature. 2014;505(7481):97-102.
12. Rafii S, Butler JM, Ding B-S. Angiocrine functions of organ-specific endothelial cells. Nature. 2016;529(7586):316-25.
13. Rivas-Carrillo SD, Kanamune J, Iwanaga Y, Uemoto S, Daneri-Navarro A, Rivas-Carrillo JD. Endothelial Cells Promote Pancreatic Stem Cell Activation During Islet Regeneration in Mice. Transplantation Proceedings. 2011;43(9):3209-11.

14. Perochon J, Yu Y, Aughey GN, Medina AB, Southall TD, Cordero JB. Dynamic adult tracheal plasticity drives stem cell adaptation to changes in intestinal homeostasis in Drosophila. Nature Cell Biology. 2021;23(5):485-96.
15. Tamamouna V, Rahman MM, Petersson M, Charalambous I, Kux K, Mainor H, et al. Remodelling of oxygen-transporting tracheoles drives intestinal regeneration and tumorigenesis in Drosophila. Nature Cell Biology. 2021;23(5):497-510.
16. Gerit, Jacobson J, Karl, Hudry B, Christo, Dormann D, et al. Neuronal Control of Metabolism through Nutrient-Dependent Modulation of Tracheal Branching. Cell. 2014;156(1-2):69-83.
17. Blackie L, Gaspar P, Mosleh S, Lushchak O, Kong L, Jin Y, et al. The sex of organ geometry. Nature. 2024;630(8016):392-400.
18. Kam CY, Singh ID, Gonzalez DG, Matte-Martone C, Solá P, Solanas G, et al. Mechanisms of skin vascular maturation and maintenance captured by longitudinal imaging of live mice. Cell. 2023;186(11):2345-60.e16.
19. Kong W, Loison O, Chavadimane Shivakumar P, Chan EH, Saadaoui M, Collinet C, et al. Experimental validation of force inference in epithelia from cell to tissue scale. Scientific Reports. 2019;9(1).
20. Ichijo R, Kabata M, Kidoya H, Muramatsu F, Ishibashi R, Abe K, et al. Vasculature-driven stem cell population coordinates tissue scaling in dynamic organs. Science Advances. 2021;7(7):eabd2575.
21. Ghabrial A, Luschnig S, Metzstein MM, Krasnow MA. Branching Morphogenesis of the Drosophila Tracheal System. Annual Review of Cell and Developmental Biology. 2003;19(Volume 19, 2003):623-47.
22. Centanin L, Gorr TA, Wappner P. Tracheal remodelling in response to hypoxia. Journal of Insect Physiology. 2010;56(5):447-54.
23. Eilken HM, Adams RH. Dynamics of endothelial cell behavior in sprouting angiogenesis. Current Opinion in Cell Biology. 2010;22(5):617-25.
24. Affolter M, Bellusci S, Itoh N, Shilo B, Thiery J-P, Werb Z. Tube or Not Tube. Developmental Cell. 2003;4(1):11-8.
25. Hayashi S, Kondo T. Development and Function of the *Drosophila* Tracheal System. Genetics. 2018;209(2):367-80.
26. Amcheslavsky A, Jiang J, Ip YT. Tissue Damage-Induced Intestinal Stem Cell Division in Drosophila. Cell Stem Cell. 2009;4(1):49-61.
27. Biteau B, Jasper H. EGF signaling regulates the proliferation of intestinal stem cells in *Drosophila*. Development. 2011;138(6):1045-55.
28. Farnsworth RH, Lackmann M, Achen MG, Stacker SA. Vascular remodeling in cancer. Oncogene. 2014;33(27):3496-505.
29. Osol G, Moore LG. Maternal Uterine Vascular Remodeling During Pregnancy. Microcirculation. 2014;21(1):38-47.
30. Spradley FT, Ge Y, Granger JP, Chade AR. Utero-placental vascular remodeling during late gestation in Sprague-Dawley rats. Pregnancy Hypertension. 2020;20:36-43.
31. Buchon N, Broderick NA, Kuraishi T, Lemaitre B. DrosophilaEGFR pathway coordinates stem cell proliferation and gut remodeling following infection. BMC Biology. 2010;8(1):152.
32. Stringer C, Wang T, Michaelos M, Pachitariu M. Cellpose: a generalist algorithm for cellular segmentation. Nature Methods. 2021;18(1):100-6.
33. Bodenschatz JFE, Ajmail K, Skamrahl M, Vache M, Gottwald J, Nehls S, et al. Epithelial cells sacrifice excess area to preserve fluidity in response to external mechanical stress. Communications Biology. 2022;5(1):855.

34. Rangamani P, Lipshtat A, Azeloglu Evren U, Calizo Rhodora C, Hu M, Ghassemi S, et al. Decoding Information in Cell Shape. Cell. 2013;154(6):1356-69.
35. He L, Si G, Huang J, Samuel ADT, Perrimon N. Mechanical regulation of stem-cell differentiation by the stretch-activated Piezo channel. Nature. 2018;555(7694):103-6.
36. Johansson J, Naszai M, Hodder MC, Pickering KA, Miller BW, Ridgway RA, et al. RAL GTPases Drive Intestinal Stem Cell Function and Regeneration through Internalization of WNT Signalosomes. Cell Stem Cell. 2019;24(4):592-607.e7.
37. Buchon N, Osman D, David FPA, Fang HY, Boquete J-P, Deplancke B, et al. Morphological and molecular characterization of adult midgut compartmentalization in Drosophila. Cell Reports. 2013;3(5):1725-38.
38. Marianes A, Spradling AC. Physiological and stem cell compartmentalization within the Drosophila midgut. Elife. 2013;2:e00886.
39. Feinberg EH, Vanhoven MK, Bendesky A, Wang G, Fetter RD, Shen K, et al. GFP Reconstitution Across Synaptic Partners (GRASP) Defines Cell Contacts and Synapses in Living Nervous Systems. Neuron. 2008;57(3):353-63.
40. Lucy, Sarah, Li X, Bilder D. Altered Modes of Stem Cell Division Drive Adaptive Intestinal Growth. Cell. 2011;147(3):603-14.
41. Schott S, Ambrosini A, Barbaste A, Benassayag C, Gracia M, Proag A, et al. A fluorescent toolkit for spatiotemporal tracking of apoptotic cells in living *Drosophila* tissues. Development. 2017;144(20):3840-6.
42. Fischer KS, Henn D, Zhao ET, Sivaraj D, Litmanovich B, Hahn WW, et al. Elevated Shear Stress Modulates Heterogenous Cellular Subpopulations to Induce Vascular Remodeling. Tissue Engineering Part A. 2024;30(23-24):752-65.
43. Sun Y, Liu J, Xu Z, Lin X, Zhang X, Li L, et al. Matrix stiffness regulates myocardial differentiation of human umbilical cord mesenchymal stem cells. Aging. 2021;13(2):2231-50.
44. Zanotelli MR, Reinhart-King CA. Mechanical Forces in Tumor Angiogenesis. Springer International Publishing; 2018. p. 91-112.
45. Negri S, Faris P, Berra-Romani R, Guerra G, Moccia F. Endothelial Transient Receptor Potential Channels and Vascular Remodeling: Extracellular Ca2 + Entry for Angiogenesis, Arteriogenesis and Vasculogenesis. Frontiers in Physiology. 2020;10.
46. Coste B, Mathur J, Schmidt M, Earley TJ, Ranade S, Petrus MJ, et al. Piezo1 and Piezo2 Are Essential Components of Distinct Mechanically Activated Cation Channels. Science. 2010;330(6000):55-60.
47. Ranade SS, Qiu Z, Woo S-H, Hur SS, Murthy SE, Cahalan SM, et al. Piezo1, a mechanically activated ion channel, is required for vascular development in mice. Proceedings of the National Academy of Sciences. 2014;111(28):10347-52.
48. Baghdadi MB, Houtekamer RM, Perrin L, Rao-Bhatia A, Whelen M, Decker L, et al. PIEZO-dependent mechanosensing is essential for intestinal stem cell fate decision and maintenance. Science. 2024;386(6725):eadj7615.
49. Kim SE, Coste B, Chadha A, Cook B, Patapoutian A. The role of Drosophila Piezo in mechanical nociception. Nature. 2012;483(7388):209-12.
50. Zechini L, Amato C, Scopelliti A, Wood W. Piezo acts as a molecular brake on wound closure to ensure effective inflammation and maintenance of epithelial integrity. Current Biology. 2022;32(16):3584-92.e4.
51. Nagarkar-Jaiswal S, Lee P-T, Campbell ME, Chen K, Anguiano-Zarate S, Cantu Gutierrez M, et al. A library of MiMICs allows tagging of genes and reversible, spatial and temporal knockdown of proteins in Drosophila. eLife. 2015;4:e05338.

52. Yang Y, Wang D, Zhang C, Yang W, Li C, Gao Z, et al. Piezo1 mediates endothelial atherogenic inflammatory responses via regulation of YAP/TAZ activation. Human Cell. 2022;35(1):51-62.
53. Lan Y, Lu J, Zhang S, Jie C, Chen C, Xiao C, et al. Piezo1-Mediated Mechanotransduction Contributes to Disturbed Flow-Induced Atherosclerotic Endothelial Inflammation. Journal of the American Heart Association. 2024;13(21):e035558.
54. Mao J, Yang R, Yuan P, Wu F, Wei Y, Nie Y, et al. Different stimuli induce endothelial dysfunction and promote atherosclerosis through the Piezo1/YAP signaling axis. Archives of Biochemistry and Biophysics. 2023;747:109755.
55. Niec RE, Chu T, Schernthanner M, Gur-Cohen S, Hidalgo L, Pasolli HA, et al. Lymphatics act as a signaling hub to regulate intestinal stem cell activity. Cell Stem Cell. 2022;29(7):1067-82.e18.
56. Wang P, Kljavin N, Nguyen TTT, Storm EE, Marsh B, Jiang J, et al. Adrenergic nerves regulate intestinal regeneration through IL-22 signaling from type 3 innate lymphoid cells. Cell Stem Cell. 2023;30(9):1166-78.e8.
57. Bernier-Latmani J, Petrova TV. Intestinal lymphatic vasculature: structure, mechanisms and functions. Nature Reviews Gastroenterology & Hepatology. 2017;14(9):510-26.
58. Bernier-Latmani J, González-Loyola A, Petrova TV. Mechanisms and functions of intestinal vascular specialization. Journal of Experimental Medicine. 2024;221(1).
59. Stzepourginski I, Nigro G, Jacob J-M, Dulauroy S, Sansonetti PJ, Eberl G, et al. CD34 $^{+}$ mesenchymal cells are a major component of the intestinal stem cells niche at homeostasis and after injury. Proceedings of the National Academy of Sciences. 2017;114(4):E506-E13.
60. McCarthy N, Manieri E, Storm EE, Saadatpour A, Luoma AM, Kapoor VN, et al. Distinct Mesenchymal Cell Populations Generate the Essential Intestinal BMP Signaling Gradient. Cell Stem Cell. 2020;26(3):391-402.e5.
61. Kim J-E, Fei L, Yin W-C, Coquenlorge S, Rao-Bhatia A, Zhang X, et al. Single cell and genetic analyses reveal conserved populations and signaling mechanisms of gastrointestinal stromal niches. Nature Communications. 2020;11(1).
62. Palikuqi B, Rispal J, Reyes EA, Vaka D, Boffelli D, Klein O. Lymphangiocrine signals are required for proper intestinal repair after cytotoxic injury. Cell Stem Cell. 2022;29(8):1262-72.e5.
63. Claxton S, Kostourou V, Jadeja S, Chambon P, Hodivala-Dilke K, Fruttiger M. Efficient, inducible Cre-recombinase activation in vascular endothelium. genesis. 2008;46(2):74-80.
64. Bernier-Latmani J, Petrova TV. High-resolution 3D analysis of mouse small-intestinal stroma. Nature Protocols. 2016;11(9):1617-29.
65. Blache P, Van De Wetering M, Duluc I, Domon C, Berta P, Freund J-NL, et al. SOX9 is an intestine crypt transcription factor, is regulated by the Wnt pathway, and represses the *CDX2* and *MUC2* genes. The Journal of Cell Biology. 2004;166(1):37-47.
66. Liu L, Rao JN, Zou T, Xiao L, Smith A, Zhuang R, et al. Activation of Wnt3a signaling stimulates intestinal epithelial repair by promoting c-Myc-regulated gene expression. American Journal of Physiology-Cell Physiology. 2012;302(1):C277-C85.
67. Cordero JB, Ridgway RA, Valeri N, Nixon C, Frame MC, Muller WJ, et al. c-Src drives intestinal regeneration and transformation. The EMBO Journal. 2014.

68. Chen P, Zhang G, Jiang S, Ning Y, Deng B, Pan X, et al. Mechanosensitive Piezo1 in endothelial cells promotes angiogenesis to support bone fracture repair. Cell Calcium. 2021;97:102431.
69. Kang H, Hong Z, Zhong M, Klomp J, Bayless KJ, Mehta D, et al. Piezo1 mediates angiogenesis through activation of MT1-MMP signaling. American Journal of Physiology-Cell Physiology. 2019;316(1):C92-C103.
70. Peralta M, Dupas A, Larnicol A, Lefebvre O, Goswami R, Stemmelen T, et al. Endothelial calcium firing mediates the extravasation of metastatic tumor cells. iScience. 2025;28(2):111690.
71. Boeldt DS, Bird IM. Vascular adaptation in pregnancy and endothelial dysfunction in preeclampsia. Journal of Endocrinology. 2017;232(1):R27-R44.
72. Guelfi S, Hodivala-Dilke K, Bergers G. Targeting the tumour vasculature: from vessel destruction to promotion. Nature Reviews Cancer. 2024;24(10):655-75.
73. Roux E, Bougaran P, Dufourcq P, Couffinhal T. Fluid Shear Stress Sensing by the Endothelial Layer. Frontiers in Physiology. 2020;11.
74. Fraisl P, Mazzone M, Schmidt T, Carmeliet P. Regulation of Angiogenesis by Oxygen and Metabolism. Developmental Cell. 2009;16(2):167-79.
75. Gervais L, Bardin AJ. Tracheal remodelling supports stem cells. Nature Cell Biology. 2021;23(6):580-2.
76. Fortuño A, José GS, Moreno MU, Díez J, Zalba G. Oxidative stress and vascular remodelling. Experimental Physiology. 2005;90(4):457-62.
77. Centanin L, Dekanty A, Romero N, Irisarri M, Gorr TA, Wappner P. Cell Autonomy of HIF Effects in Drosophila: Tracheal Cells Sense Hypoxia and Induce Terminal Branch Sprouting. Developmental Cell. 2008;14(4):547-58.
78. Mukherjee P, El-Abbadi MM, Kasperzyk JL, Ranes MK, Seyfried TN. Dietary restriction reduces angiogenesis and growth in an orthotopic mouse brain tumour model. British Journal of Cancer. 2002;86(10):1615-21.
79. Matamoro-Vidal A, Cumming T, Davidović A, Levillayer F, Levayer R. Patterned apoptosis has an instructive role for local growth and tissue shape regulation in a fast-growing epithelium. Current Biology. 2024;34(2):376-88.e7.
80. Roellig D, Theis S, Proag A, Allio G, Bénazéraf B, Gros J, et al. Force-generating apoptotic cells orchestrate avian neural tube bending. Developmental Cell. 2022;57(6):707-18.e6.
81. Kawaue T, Yow I, Pan Y, Le AP, Lou Y, Loberas M, et al. Inhomogeneous mechanotransduction defines the spatial pattern of apoptosis-induced compensatory proliferation. Developmental Cell. 2023;58(4):267-77.e5.
82. Yui S, Azzolin L, Maimets M, Pedersen MT, Fordham RP, Hansen SL, et al. YAP/TAZ-Dependent Reprogramming of Colonic Epithelium Links ECM Remodeling to Tissue Regeneration. Cell Stem Cell. 2018;22(1):35-49.e7.
83. Ciccone G, Azevedo Gonzalez Oliva M, Antonovaite N, Lüchtefeld I, Salmeron-Sanchez M, Vassalli M. Experimental and Data Analysis Workflow for Soft Matter Nanoindentation. Journal of Visualized Experiments. 2022(179).
84. Marchetti M, Zhang C, Edgar BA. An improved organ explant culture method reveals stem cell lineage dynamics in the adult Drosophila intestine. eLife. 2022;11:e76010.
85. Martin JL, Sanders EN, Moreno-Roman P, Jaramillo Koyama LA, Balachandra S, Du X, et al. Long-term live imaging of the Drosophila adult midgut reveals real-time dynamics of division, differentiation and loss. eLife. 2018;7:e36248.

86. Herbert S, Valon L, Mancini L, Dray N, Caldarelli P, Gros J, et al. LocalZProjector and DeProj: a toolbox for local 2D projection and accurate morphometrics of large 3D microscopy images. BMC Biology. 2021;19(1).
87. Aigouy B, Umetsu D, Eaton S. Segmentation and Quantitative Analysis of Epithelial Tissues. Springer New York; 2016. p. 227-39.
88. Newton H, Wang YF, Camplese L, Mokochinski JB, Kramer HB, Brown AEX, et al. Systemic muscle wasting and coordinated tumour response drive tumourigenesis. Nat Commun. 2020;11(1):4653.
89. Gervais L, Casanova J. The Drosophila homologue of SRF acts as a boosting mechanism to sustain FGF-induced terminal branching in the tracheal system. Development. 2011;138(7):1269-74.
90. Goto S, Hayashi S. Proximal to distal cell communication in the Drosophila leg provides a basis for an intercalary mechanism of limb patterning. Development. 1999;126(15):3407-13.
91. Fletcher GC, Diaz-de-la-Loza MD, Borreguero-Muñoz N, Holder M, Aguilar-Aragon M, Thompson BJ. Mechanical strain regulates the Hippo pathway in Drosophila. Development. 2018;145(5).
92. Roy S, Huang H, Liu S, Kornberg TB. Cytoneme-mediated contact-dependent transport of the Drosophila decapentaplegic signaling protein. Science. 2014;343(6173):1244624.
93. Yagi R, Mayer F, Basler K. Refined LexA transactivators and their use in combination with the *Drosophila* Gal4 system. Proceedings of the National Academy of Sciences. 2010;107(37):16166-71.

**Acknowledgements:**

We would like to thank Norbert Perrimon (Harvard), Irene Miguel-Aliaga (The Francis Crick Institute), Shigeo Hayashi (Rinken Centre, Kobe, Japan), Chrysoula Pitsouli (University of Cyprus), Thomas Kornberg and Wanpeng Wang (Kornberg Lab-UCSF), Barry Denholm (University of Edinburgh), Barry Thompson (EMBL Australia), Gines Morata (Autonomous University of Madrid), Lucy O'Brien (Stanford University), Susumu Hirabayashi (Imperial College London), Magali Suzanne (CBI Toulouse), Yanlan Mao (UCL) and Andrew Davidson (University of Glasgow) for generously sharing flies and reagents, and Marcus Fruttiger (UCL) for sharing the *Pdgf-beta-Cre-GFP* mice. We thank the Bloomington Drosophila Stock Centre; the Vienna Drosophila Resource Center and the *Drosophila* Studies Hybridoma Bank for fly stocks and antibodies. We would like to thank the Core Services and Advanced Technologies at the CRUK Scotland Institute, which is core funded by Cancer Research UK (A31287). With particular thanks to Leo Carlin, Claire Mitchell, and Peter Thomason from the Beatson Advanced Imaging Resource for imaging support, Derek Miller and Evarest Onwubiko from the Biological Service Unit for assistance with animal whole body perfusions for whole mount intestinal sample preparations, and Dimitris Athineos and Dale Watt for assistance with stock maintenance and back crossing of the *Piezo1*$^{fl/fl}$ mice. We are grateful to Jeremiah Bernier-Latmani and Tatiana Petrova for their support and advice during intestinal vascular tissue preparation and imaging. The manuscript was critically reviewed by Catherine Winchester (CRUK Scotland Institute). We thank all members of the Cordero laboratory for general advice on the project.

**Data availability:** All source data related to this study will be made freely available through institutional public repositories and accessible via a DOI link at the time of publication.

**Funding sources:** Work in the Cordero laboratory is funded through a Wellcome Trust and Royal Society Sir Henry Dale Fellowship (104103/Z/14/Z), Wellcome Senior Research Fellowship (223091/Z/21/Z) and core Institutional funds from CRUK to the CRUK Scotland Institute (A31287) to J.B.C., a Wellcome ISSF Returner Scheme (204820/Z/16/Z) and Tenovus (Tenovus/S22-28) Fellowships to J.P, and an

EPSRC/MVLS studentship to C.J. (A31GA-7101). The Blyth laboratory is supported by CRUK funding (A29799) to K.B. Work from the Vassalli laboratory is supported by Leverhulme Trust grant RPG-2022-324 and EPSRC grant Mechanomeds EP/X033554 to M.V.

**Authors contributions:**

J.A.P. Designed, performed and analysed experiments, including all the work on tissue segmentation and morphometric analysis, and mouse experiments.

J.P. Designed, performed and analysed experiments, including the study of signalling mechanisms downstream of Piezo. Contributed to study conceptualization, supervision and funding acquisition.

C.T.J. Designed, performed and analysed experiments involving the use of Chiaro nanoindenter, and the time course of Piezo expression and activation.

M.W. Provided training and assistance with nanoindentation data acquisition and analysis.

C. N. and M.H. Processed samples for mammalian histology.

A.B.C. Contributed to early efforts in live imaging.

Y.Y. Provided general technical assistance and generated the *lexAop-Src* line.

L.M and K.B. Provided support with the supervision and planning of the mouse work.

M.V. Planning, supervision and analysis of nanoindentation work and funding acquisition.

J.B.C. Study conceptualization, supervision, data analysis and funding acquisition.

J.A.P., J.P., C.T.J, and J.B.C., Wrote the manuscript with input from the rest of the authors.

**Conflict of Interests:** The authors declare no conflict of interests.

1532

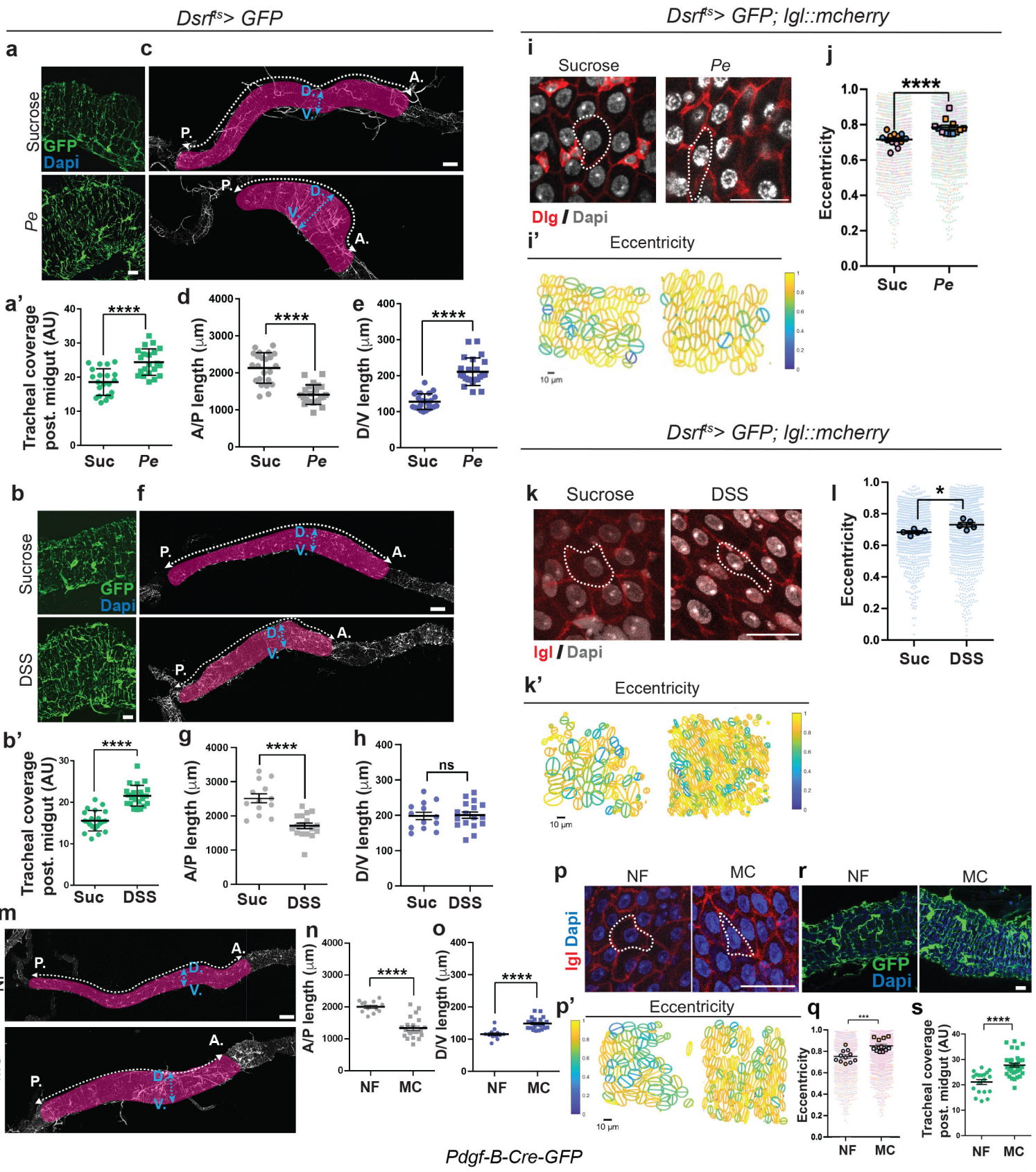


Phillips and Perochon et al. Figure 1

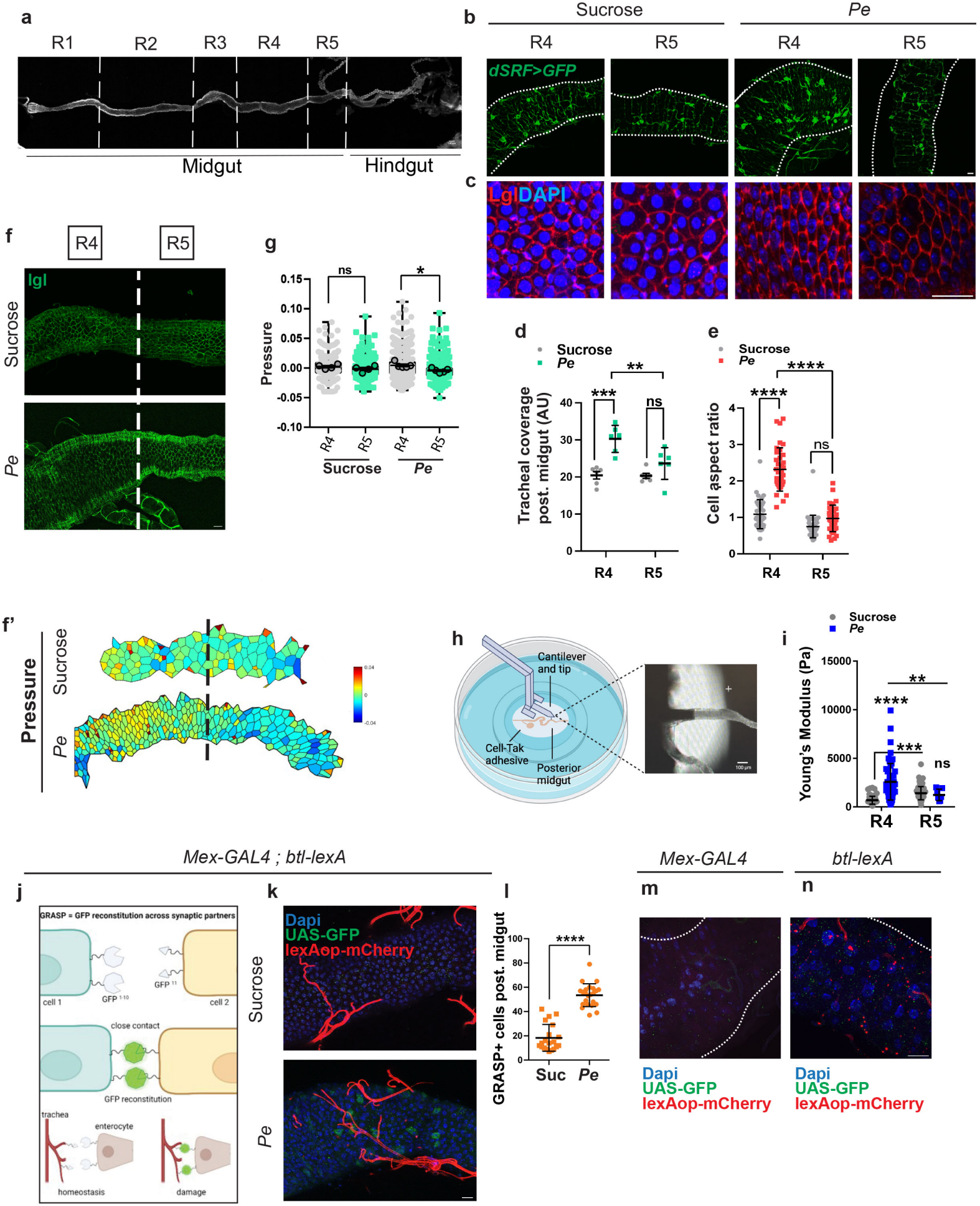


Phillips and Perochon et al. Figure 2

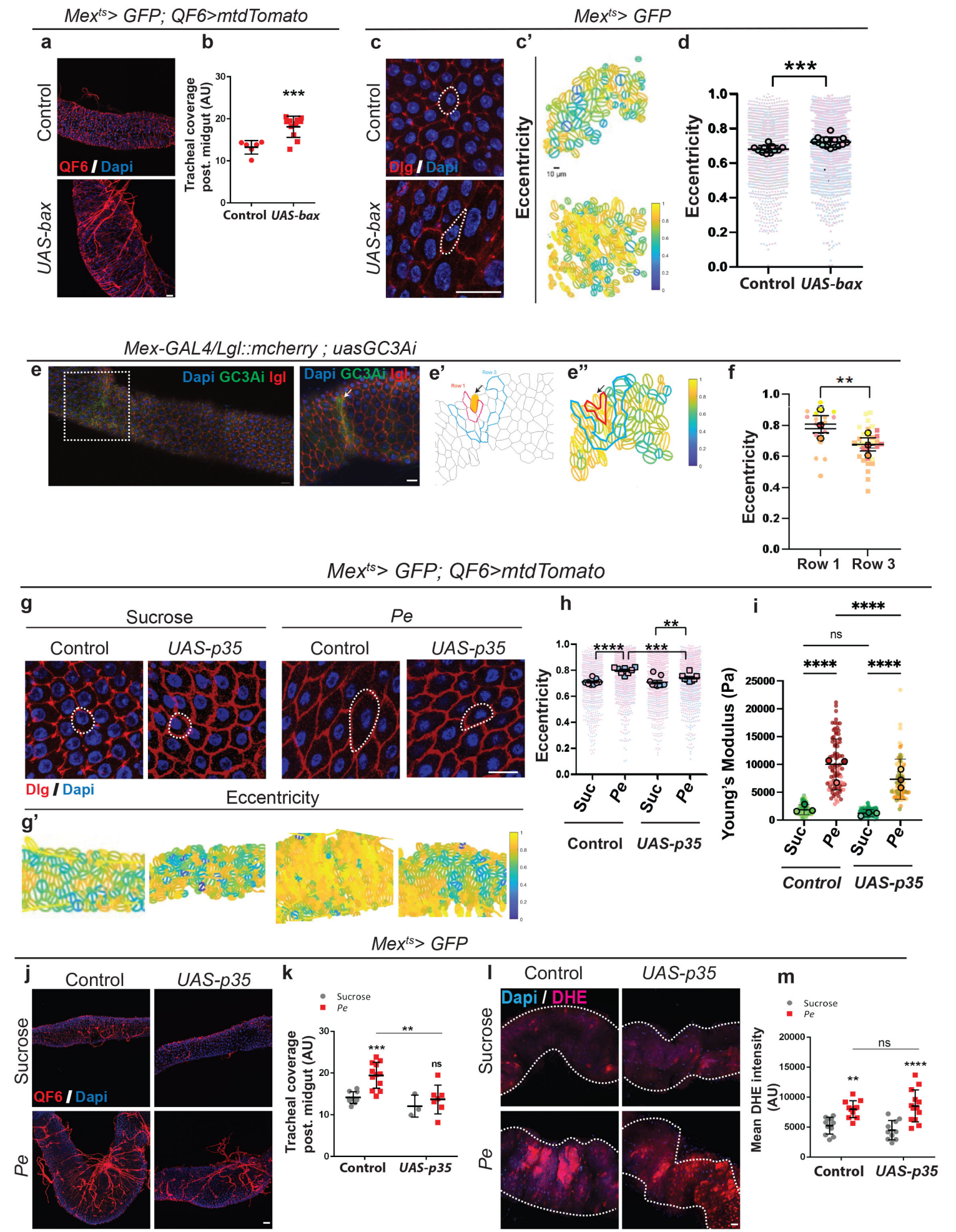


Phillips and Perochon et al. Figure 3

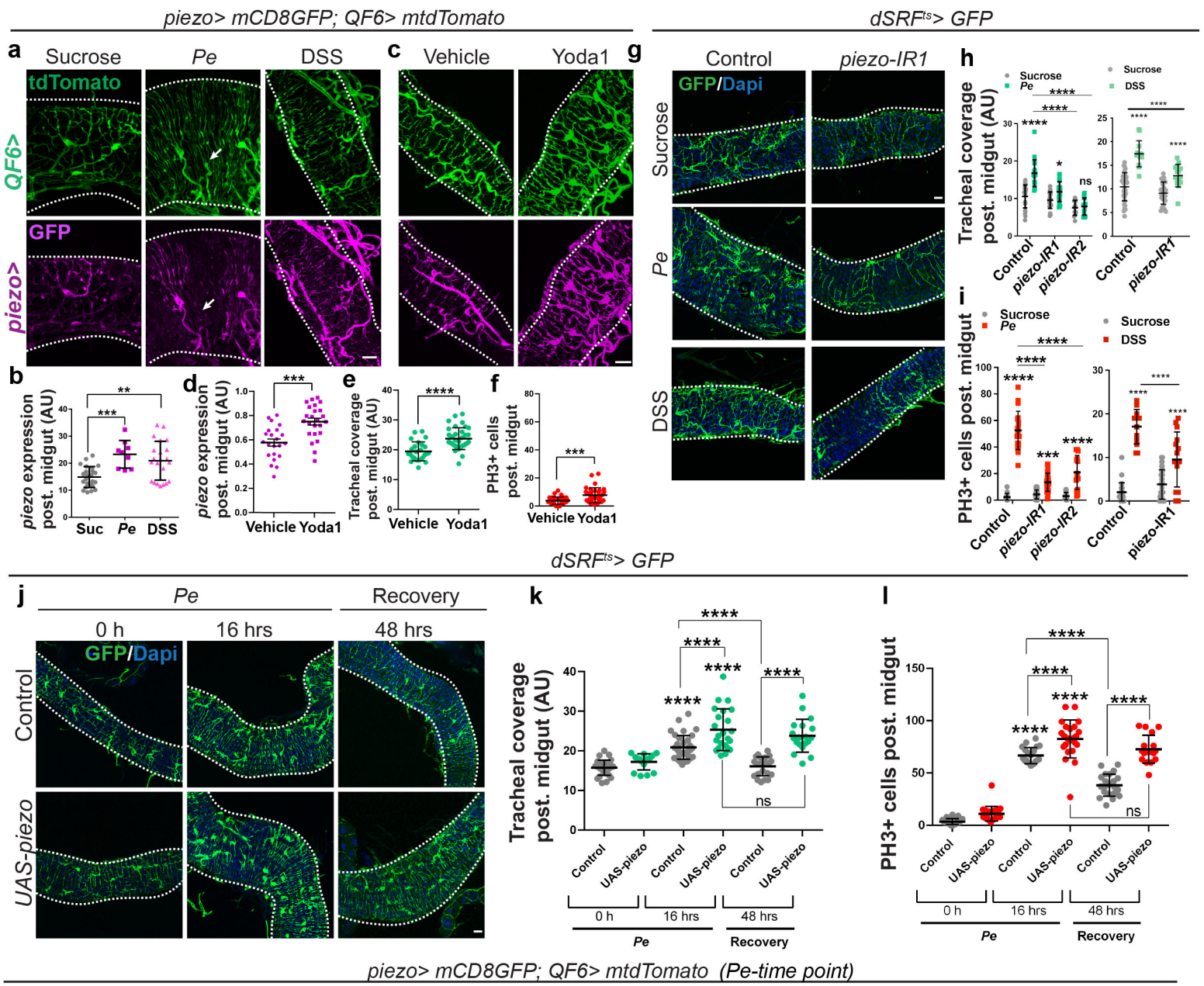


Phillips and Perochon et al. Figure 4

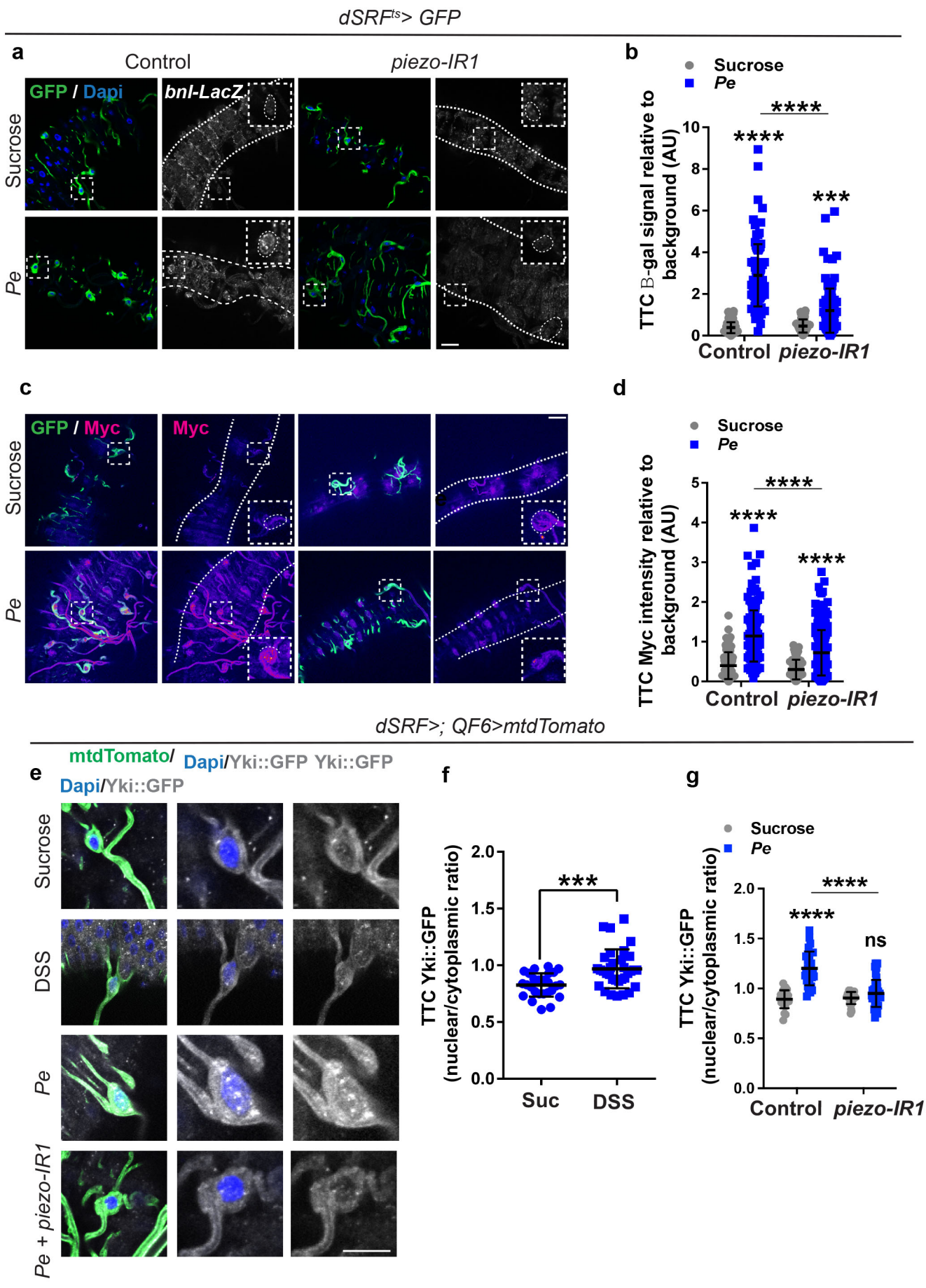


Phillips and Perochon et al. Figure 5

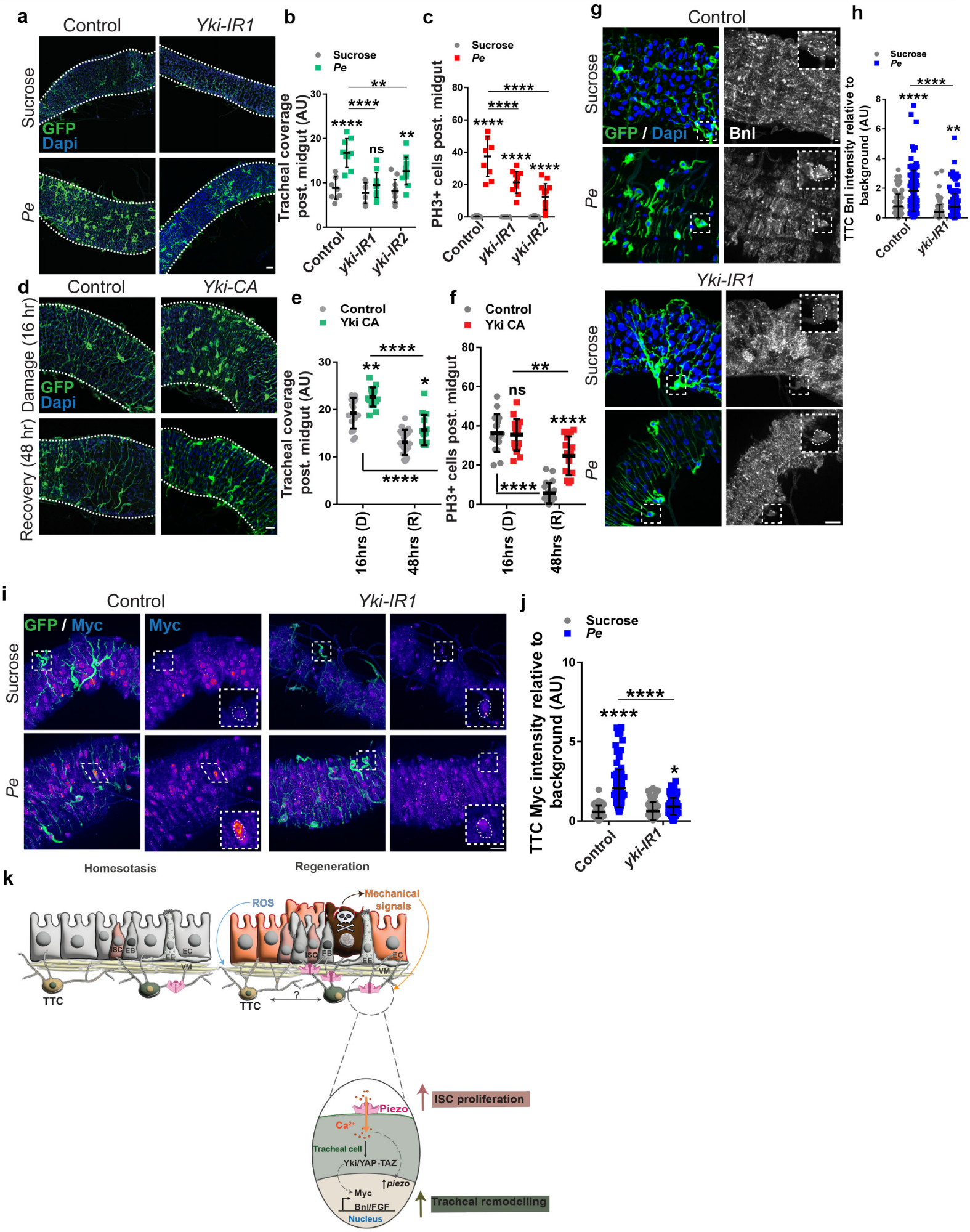


Phillips and Perochon et al. Figure 6

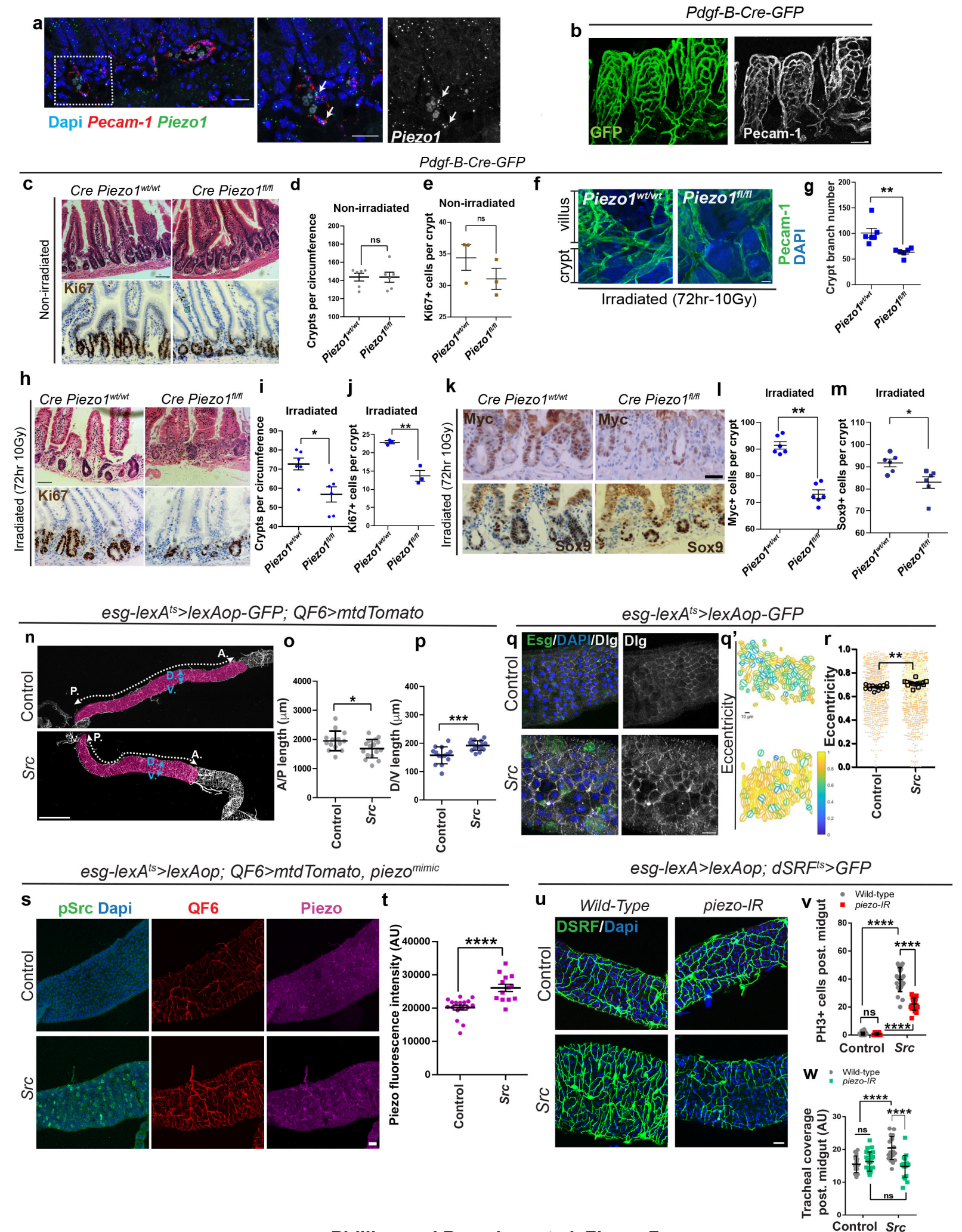


Phillips and Perochon et al. Figure 7

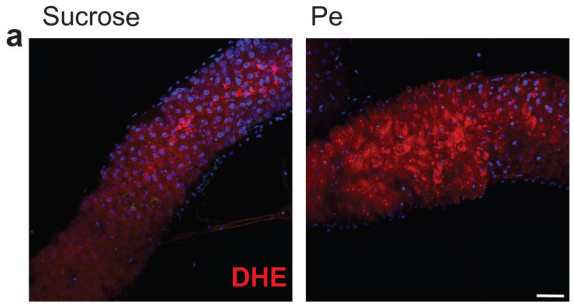


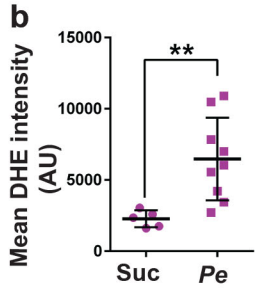


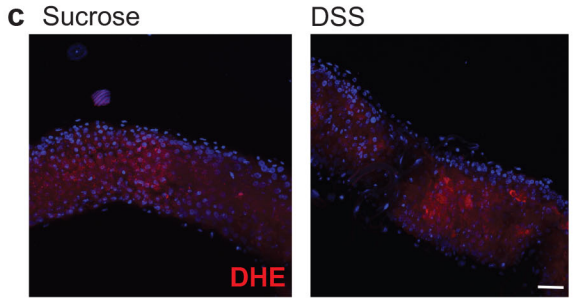


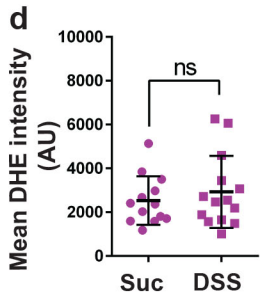


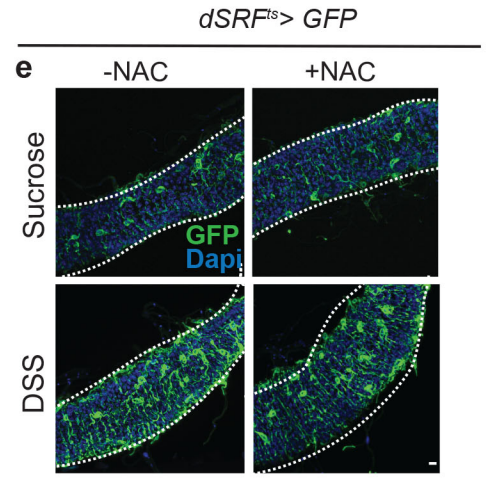


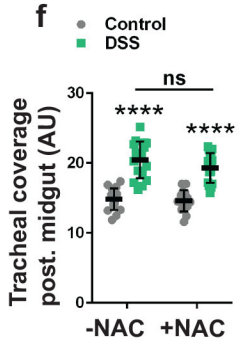


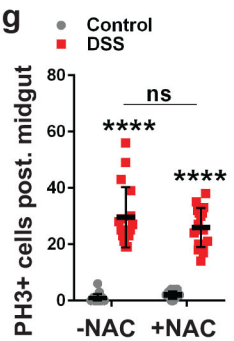


**Phillips and Perochon et al. Extended data Fig. 1**

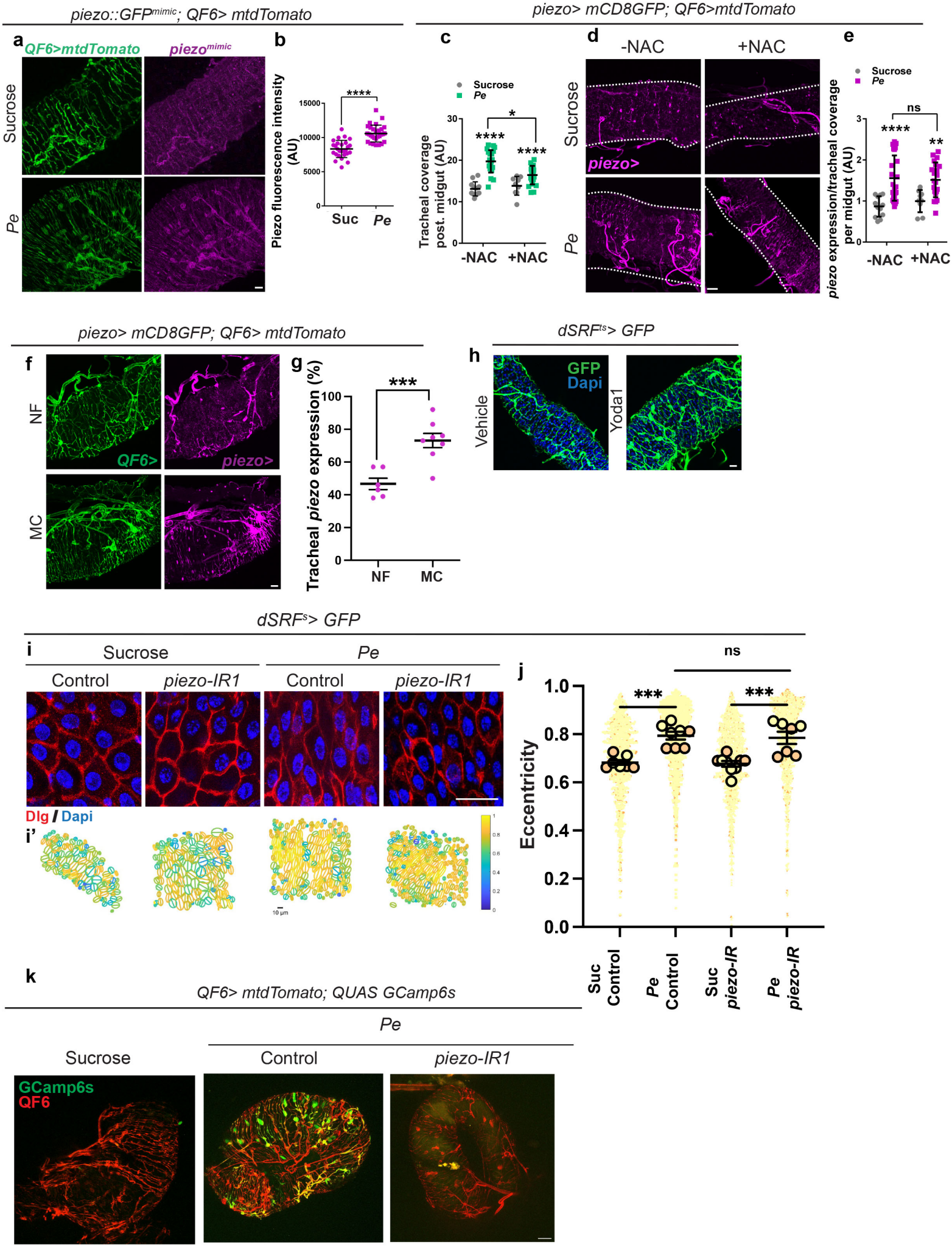


**Phillips and Perochon et al. Extended data Fig. 2**

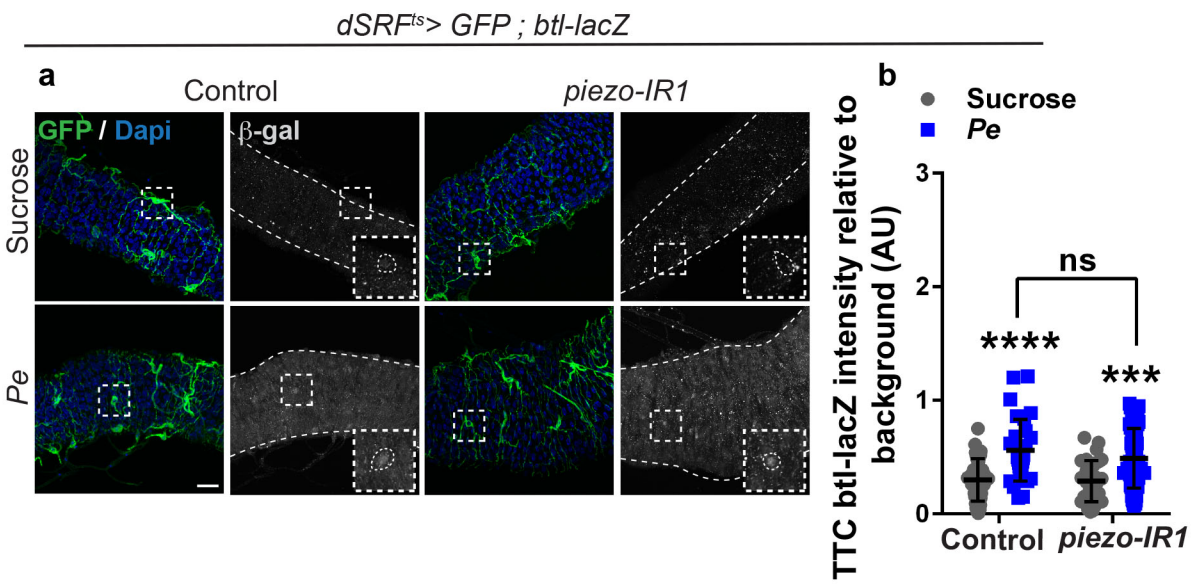


Phillips and Perochon et al. Extended data Figure 3

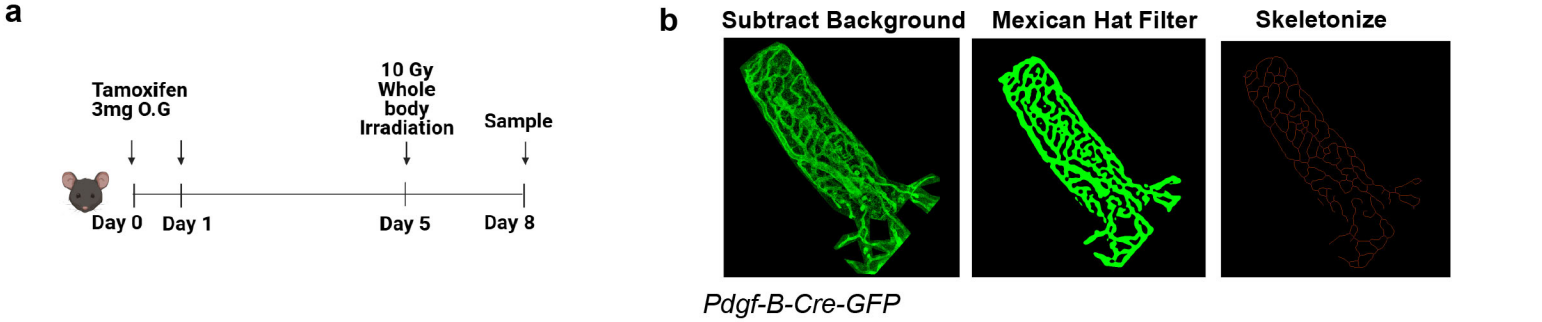


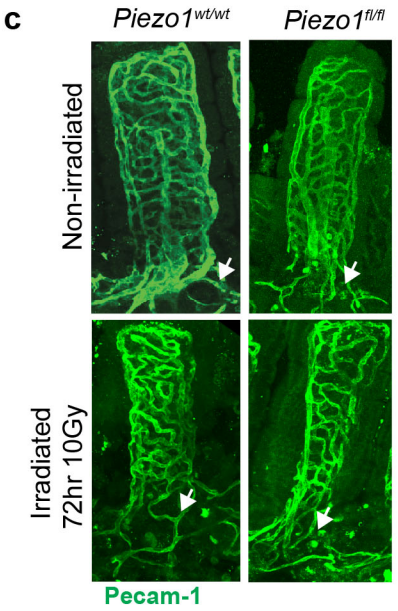


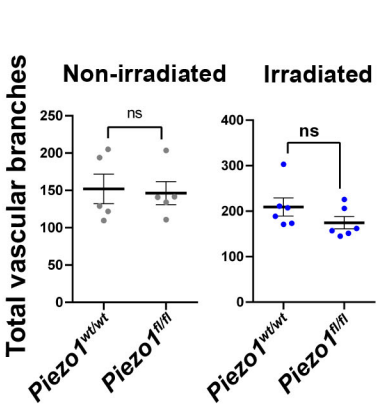


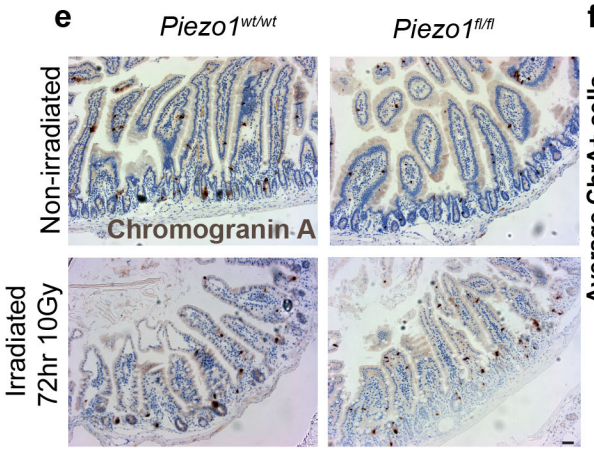


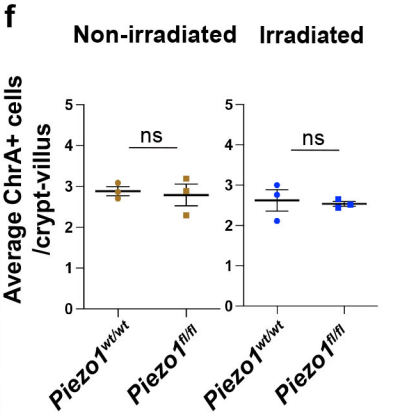


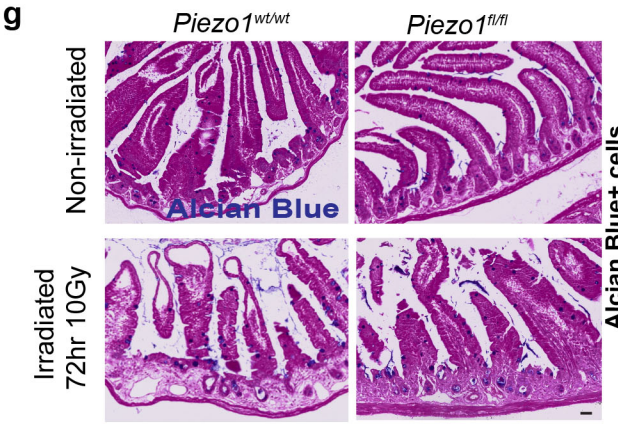


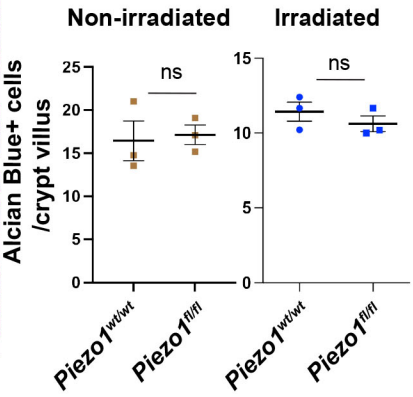


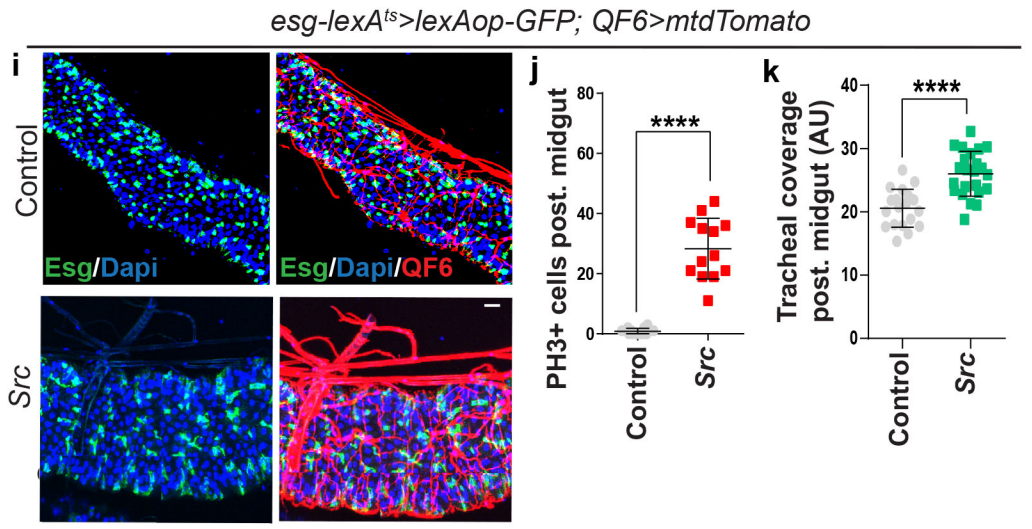


Phillips and Perochon et al. Extended data Fig. 4